Catalysis Communications 179 (2023) 106681

Contents lists available at ScienceDirect

Catalysis Communications

journal homepage: www.elsevier.com/locate/catcom

UV–vis light responsive Bi_2WO_6 nanosheet/TiO_2 nanobelt heterojunction photo-catalyst for CO_2 reduction

Maryam Ahmadi [a], Seyed Mehdi Alavi [a,*], Afsanehsadat Larimi [b,*]

[a] Catalyst and Nanomaterials Research Laboratory (CNMRL), School of Chemical, Petroleum and Gas Engineering, Iran University of Science and Technology, Tehran, Iran

[b] Department of Chemical and Process Engineering, Niroo Research Institute, Tehran, Iran

ARTICLE INFO

Keywords:
Bi_2WO_6
TiO_2
Photocatalyst
CO_2 conversion

ABSTRACT

A series of Bi_2WO_6/TiO_2 composite photocatalysts with different ratios of Bi_2WO_6 nanosheets to TiO_2 nanobelts (1, ½, $^1/_3$ and ¼) were synthesized by hydrothermal method and evaluated for CO_2 photoreduction. The structural and optical properties of these photocatalysts were investigated by XRD, N_2-physisorption, EDX, FESEM, Raman, TPD, DRS and PL. Bi_2WO_6/TiO_2 composite photocatalysts show enhanced CO_2 adsorption capacity and coversion performance compared to both pure TiO_2 and bulk Bi_2WO_6. Loading Bi_2WO_6 nanosheets on TiO_2 nanobelts leads to formation a heterojunction, which enhances the photocatalytic visible light performance by decreasing the recombination rate of photoinduced electron-hole pairs. The maximum CH_4 production of 18.95 $\mu mol/g_{cat}$ in 8 h has been reported for composite with Bi_2WO_6/TiO_2 ratio of ½, which is 3 times higher than that of bulk Bi_2WO_6 and pure TiO_2.

1. Introduction

Recent increase in fossil fuel consumption results in enhanced CO_2 emission which in turn contributes to the global warming and consequent climate changes [1,2]. Thus, developing efficient strategies for CO_2 capture, storage, and utilization would be of great interest [3]. Meanwhile, human society should focus on finding renewable sources of energy with closed carbon cycle for the future [4,5]. In this regard, photoreduction of CO_2 into hydrocarbons such as CH_4 or CH_3OH has got much attention because of several advantages: 1) clean and abundant solar energy can be used as the source of energy in this reaction; 2) untreated CO_2 and water from human activities can be used as reaction reactants; 3) this reaction commonly can drive at mild operational conditions [6,7].

The photocatalytic conversion of carbon dioxide by into value-added hydrocarbons was first investigated in 1978 [1]. The bandgap energy and photocatalyst nature are two important factors determining the photocatalyst performance. Developing efficient systems for the photocatalytic reduction of CO_2 in the presence of solar energy is a highly desirable, still challenging goal [8–10]. A variety of semiconductors and metal complexes have been investigated as photocatalysts for CO_2 reduction under visible light irradiation. The metal oxide photocatalysts show excellent chemical stability for CO_2 photoreduction [11–15], among them TiO_2-based photocatalysts have widely applied for photocatalytic reaction because of chemical stability, low coast, non-toxicity and availability [16–19]. However, TiO_2 comes with its own limitations including low specific surface area, weak CO_2 adsorption and wide bandgap. However, from the energy consumption point of, it is important to provide an effective photocatalyst that can reduce CO_2 under visible light, which means the need for narrow band gaps [19,20]. In this venue, various techniques like doping metals and non-metals [21,22], coupling with other semiconductors [13,23,24], and surface modification [25,26] have been employed to reduce the bandgap of TiO_2, limit the electron-hole recombination rate and thus enhance the photoactivity in visible light region [27–30]. Structures such as nanorods, nanotubes, and nanobelts exhibit high photocatalytic performance due to their high specific surface area and low recombination rate of electron-hole carriers. These structures can provide a short distance for the migration of charge carriers to the photocatalyst surface. Thus, photoinduced charge carriers can immediately participate in reaction which in turn enhances the separation of electrons and holes. Heterojunction nanostructured photocatalysts have attracted attentions because of their low rate of recombination of photoinduced electron-hole carries [31–34]. Hence, combination of TiO_2 with other semiconductors with narrow bandgaps

* Corresponding authors.
E-mail addresses: alavi.m@iust.ac.ir (S.M. Alavi), alarimi@nri.ac.ir (A. Larimi).

https://doi.org/10.1016/j.catcom.2023.106681
Received 4 March 2023; Received in revised form 26 April 2023; Accepted 2 May 2023
Available online 3 May 2023

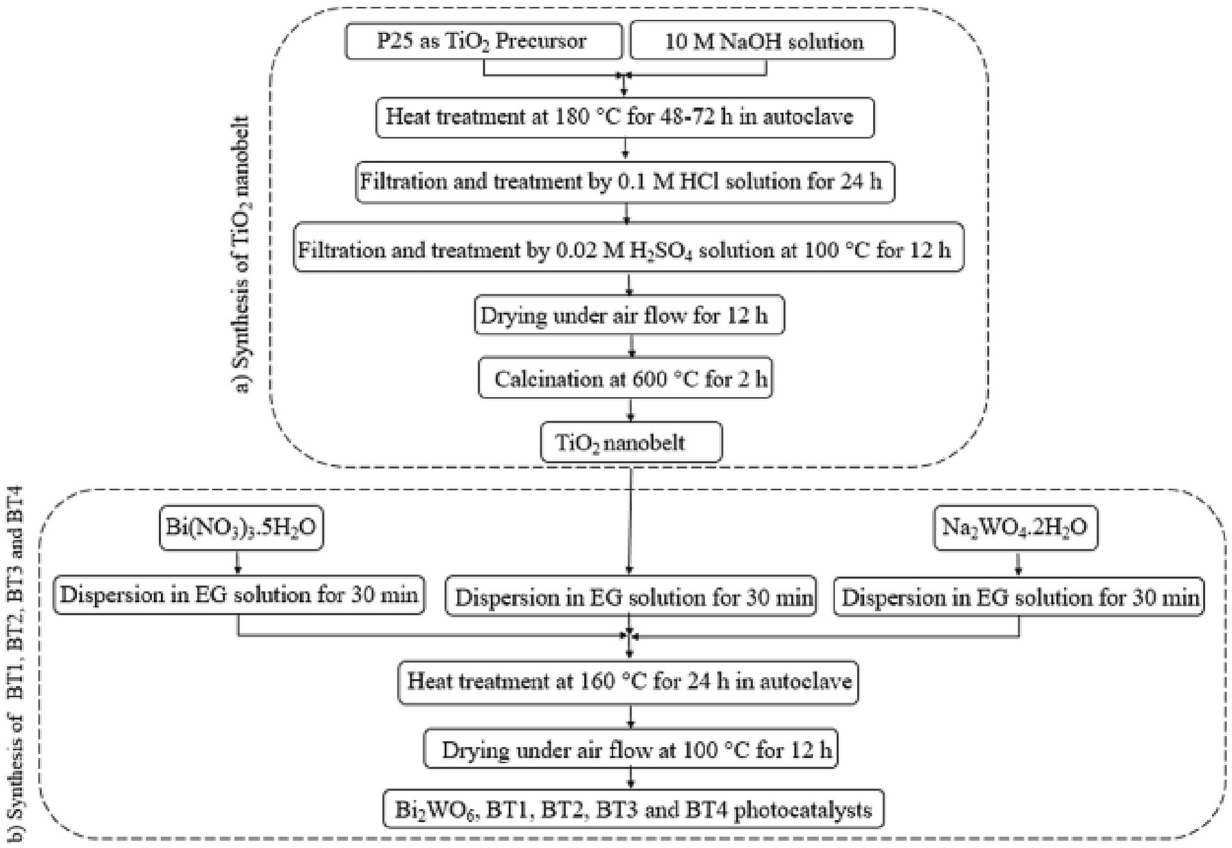

Fig. 1. Diagram of preparation steps of the Bi2WO6, TiO2, BT1, BT2, BT3 and BT4 photocatalysts.

to provide a heterojunction is an effective strategy for providing a visible light-responsible photocatalyst with low charge carrier recombination rate [35–37]. Bi_2WO_6 with narrow bandgap (2.8 e.V) has been regarded as a good candidate to make heterojunction with TiO_2 in order to reduce bandgap energy and increase the separation of photoinduced charge carriers [38,39].

It is well-known that Bismuth-containing photo-catalysts show an excellent visible light responsibility due to their low bandgap [4,40–42]. Moreover, presence of Bi in photocatalyst structure can improve adsorption and activation of CO_2 on photocatalyst surface [22]. In addition, for Bi modified TiO_2 photocatalyst, formation of $Bi_2Ti_2O_7$ is predicted to stabilize CO_2 by forming carbonate species [21]. Furthermore, incorporation of Bi in TiO_2 structure leads to formation of Bi_2O_3 which tends to absorb CO_2 molecules to form $(BiO)_2CO_3$. Bi^{3+} ions typically are considered as weak base species that can enhance the CO_2 molecules absorption capacity in Bi modified photocatalysts [43]. Recently, layered Bi_2MO_6 photocatalysts have attracted particular attention because of their exceptional structural and optical features, such as outstanding visible-light absorption [44,45], suitable band potential [46,47], and considerable chemical stability [3,48,49], [50]. The layered structure of Bi_2MO_6 (M = W, Mo) can improves the separation efficiency of photogenerated carriers and hence increase the photo-conversion performance [42]. The Bi_2WO_6 is a nontoxic, photo-stable, and thermally stable photocatalyst. These factors are essential for solar photocatalytic conversion, in particular for CO_2 photo-conversion [51]. The 2D Bi_2WO_6 thin nanosheets are of great interest as an efficient photocatalysts for CO_2 conversion because of their large specific surface area, superior electron conductivity, and charge carrier separation compared to 1D material. Ultrathin structure of this photocatalyst provides a short diffusion distance and can decrease recombination rate of photoinduced electron-holes. Therefore, the photocatalyst is predicted to show excellent performance for the photocatalytic activity. The 2D Bi_2WO_6 photocatalyst has been studied to investigate the effects of intensity of light, amount of H_2O, and photocatalyst dosage on CO_2 photoreduction process in a continuous-flow photo-reactor system. These factors have been shown to influence the CO_2 photoconversion independently. Therefore, they should be optimized to enhance the photoreduction performance [40]. The Bi_2WO_6/ACS photocatalyst has been synthesized with excellent ability for CO_2 adsorption and high efficiency of charge migration. The synergetic effect between Bi_2WO_6 and ACSs can improve the photoreduction of CO_2 with the CO yield of 57.5 μmol/g, which is about 2.25 times higher than that of the pure Bi_2WO_6 [52]. Bi_2WO_6/g-C_3N_4 and Bi_2WO_6/RGO/g-C_3N heterostructures have been developed for CO_2 photoreduction. The photoreduction activity mainly corresponds to the specific 2D/2D/2D structure of photocatalyst. This structure provides an effective interfacial contact between the constituents for efficient migration of charges and limit the direct recombination of photoinduced charge carriers [53]. A hollow structure of QDh-Bi_2WO_6 has been investigated for photoconversion of CO_2 to CH_3OH. The results showed that the three-dimensional QDh-Bi_2WO_6 photocatalysts exhibit excellent efficiency for absorption of CO_2 with a narrower bandgap with respect to the Bi_2WO_6, which resulted in CO_2 photoreduction enhancement. Thus, the three-dimensional structure increased the CO_2 photo-reduction efficiency [1]. 2D/2D Bi_2WO_6/BiOI photocatalytic system with nanosize structure has been synthesized for CO_2 photocatalytic reduction. Results show that nanosize structure and interfacial contact of Bi_2WO_6/BiOI can control the photoinduced electron-hole pairs migration and recombination rate. The results demonstrate that the heterojunction structure formed between the interfaces of BOI and BWO-OV can enhance the total CH_4 yield (18.32 μmol/g), which is 7.1 times higher than that of pure BOI [54].

Some of the recent studies in the field of organic pollutants (such as methyl orange, quinoline blue, Rhodamine B, and methylene blue) degradation show that coupling of TiO_2 with another visible light

response semiconductors like Bi_2WO_6 can form a heterojunction with lower recombination rate of photoinduced charge carriers by creating charge transfer channels between Bi_2WO_6 and TiO_2 [55,56] [57–59]. Recently investigation also show that the molar ratio of TiO_2 to Bi_2WO_6 can play an important role in morphology and crystal structure of composite photocatalyst which in turn affects the photocatalytic performance [60].

Although previous studies suggest that coupling of Bi_2WO_6 with another semiconductor like TiO_2 is an excellent method to making full use of both TiO_2 and Bi_2WO_6 advantageous characteristics, there are few works that focus on photocatalytic activity of Bi_2WO_6/TiO_2 heterostructure for CO_2 photo-reduction reaction. Thus, in this work Bi_2WO_6/TiO_2 composite photocatalysts were synthesized by hydrothermal method and employed for photocatalytic conversion of CO_2 under visible light irradiation. Effect of different molar ratios of Bi_2WO_6/TiO_2 on the photocatalytic performance were also investigated by performing a number of physicochemical characterization techniques.

2. Materials and methods

2.1. Materials

The precursors were commercial titanium dioxide (P25), sodium hydroxide (NaOH), hydrochloric acid (HCL), sulphuric acid (H_2SO_4), bismuth (III) nitrate pentahydrate [Bi $(NO_3)_3{\cdot}5H_2O$], Sodium tungstate dihydrate ($Na_2WO_4.2H_2O$), ethylene glycol ($CH_2OH)_2$ were purchased from Merck and used without any purification. Deionized water were used as solvent in this study.

2.2. Preparation of photocatalysts

Fig. 1 shows the synthesis procedure of the Bi_2WO_6/TiO_2 samples.

2.2.1. Fabrication of TiO_2 nanobelts

First 0.4 g P25 was added into 80 mL of 1 mol/L sodium hydroxide (NaOH) solution and dispersed under magnitude stirring for 1 h. The prepared suspension was then transferred into a 120 mL Teflon lined autoclave and heated at 180 °C for 48 h. Then prepared gel was filtered and after that washed 2 times with pure water. Afterward, the obtained solid was immersed in hydrochloric acid solution (0.1 M) for 24 h. The resulting solid was filtered. Then, filtered solid was dispersed in H_2SO_4 solution (0.02 M) at 100 °C for 12 h in a 120 mL Teflon container. The sample was filtered and after that washed several times with deionized water. Then nanobelts was dried at 100 °C for 12 h and finally calcinated at 600 °C for 2 h.

2.2.2. Synthesis of Bi_2WO_6/TiO_2

2 mmol of Bismuth (III) nitrate pentahydrate ($Bi(NO_3)_3{\cdot}5H_2O$) and 1 mmol of Sodium tungstate dihydrate ($Na_2WO_4.2H_2O$) separately were dissolved in 20 mL ethylene glycol (EG) and then stirred for half of hour at room temperature (solution A and B, respectively). An appropriate amount (1, 2, 3 or 4 mmol) of as-synthesized TiO_2 nanobelts was immersed in 20 mL ethylene glycol (EG) for 30 min (solution C). Then, the three last solutions (A, B, C) were mixed and transferred into a 120 mL stainless steel autoclave to treat at 160 °C for 24 h. Finally, the resulting solids were collected and washed with deionized water. Then obtained solid was dried at 100 °C for 12 h. Bi_2WO_6/TiO_2 samples that were synthesized using 1, 2, 3 and 4 mmol of TiO_2 nanobelts named BT1, BT2, BT3 and BT4, respectively. The pure Bi_2WO_6 nanosheets also were synthesized for comparison with composites by a similar process without TiO_2 nanobelts.

2.3. Characterization techniques

The crystal structures of as-prepared samples were characterized by X-ray diffraction (XRD) using PANalytical X'PERT PRO by graphite monochromatic copper radiation (Cu Kα) in a scanning range of $2\theta = 10–90°$. The conventional diffractograms were detected by JCPDS files of components. The as-prepared photocatalysts N_2 adsorption-desorption isotherms were obtained at 77 K on BEL-sorp mini II instrument by Brunauer-Emmett-Teller (BET) method. The morphological properties of the photocatalysts were determined by field emission scanning electron microscope (FESEM) using a Mira-III Tuscan operated at 20 kV. The elemental compositions were characterized by energy-dispersive X-ray spectroscopy (EDX). The UV–Vis diffuse reflectance spectra (DRS) of as-synthesized photocatalysts were recorded on an Ava spec-2048 UV–Vis spectrophotometer with $BaSO_4$ standard reference in range of 300–800 nm. The bandgap of the samples was calculated by Kubelka-Munk equation and using Tauc method. For CO_2-TPD, 300 mg of the sample was treated at 250 °C for 1 h and then cooled down to ambient temperature. The photocatalyst was then exposed to a CO_2 stream (15 mL/min) for 45 min. The weakly amount of adsorbed CO_2 removed by flushing in helium gas (15 mL/min) for 15 min. After that, CO_2 desorption isotherms were performed by rising the operation temperature up to 700 °C under helium flow with a ramp rate of 10 °C/min. Photoluminescence (PL) spectra of samples were obtained using Agilent G9800A at room temperature and 290 nm excitation wavelength. Raman spectra of as-prepared photocatalysts were collected with a Tak-Ram-N1–541 Raman spectrometer with a 532 nm laser source.

2.4. Experimental setup for catalytic performance test

The reaction was performed under simulated UV–visible light at 1 bar and 25 °C. The experimental tests were carried out in a 200 mL prix container. The photoreactor was subjected using UV–visible 250 W mercury vapor lamps (HQL) with average irradiance of 280 W/m^2 [21]. The photoreactor has a quartz window that provide transmission of UV light from the lamp to a thin layer of photocatalysts. In each experiment, 100 mg photocatalyst was dispersed in 20 mL deionized water and was coated uniformly as a thin layer on the glass plate and placed in the central region of the photoreactor. Before the photocatalytic tests, the setup was degassed by high-purity nitrogen several times to remove all other gas species, and then refilled with carbon dioxide in each run. Then, high purity carbon dioxide flow gas (99.99% purity) was continuously injected into the photo-reactor for 30 min. The CO_2 flow gas purged air and possible gas impurities from inside the photoreactor. Then CO_2 gas passed through a water saturator for 30 min to reach the equilibrium state. Water acts as the electron donor in reaction. Then, the photoreactor was sealed, and irradiated by UV–visible light. After 12 h of irradiation to analysis of reaction product, 1 mL of gas was collected from the photoreactor using a gas tight syringe. The gas sample was injected to a Shimadzu-2010 gas chromatography with BP-5 column gas chromatography system equipped with a flame ionized detector (FID). Gas chromatograph with a flame ionization detector (FID) was carried out to detect CH_4 yield in the reactor. The schematic diagram of the reaction set-up is shown in Fig. S1. It should be noted that apart from CH_4, other products were not detected within the detection limits of our instrument or due to low amount of them. Each sample was tested two times under adjusted conditions to assure measured CH_4 product. CH_4 production yield was determined according to the following equation:

$$CH_4\ \text{yield} = \frac{\text{amount of methane produced (μmol)}}{\text{weight of photocatalyst (g)}} \quad (1)$$

The CO_2 photocatalytic reduction performance can also be measured by apparat quantum yield (AQY) [61] (Details can be found in Supporting Information). Furthermore, a number of blank experiments were performed to determine the CO_2 photocatalytic conversion products in the present system. The performance of system was investigated in the absence of photocatalyst, irradiation, CO_2 and H_2O, respectively. No products were determined using the GC system in all the blank experiments. In addition, to ensure the reliability of photocatalytic test results, each experiment was repeated 3 times in similar experimental

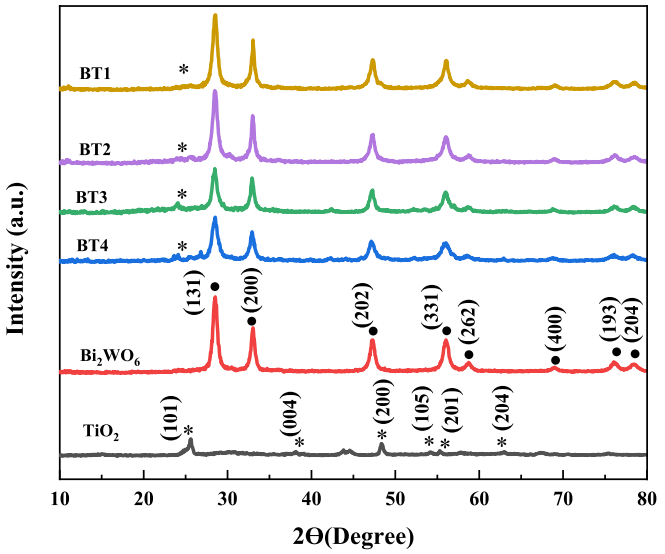

Fig. 2. XRD patterns of Bi2WO6, TiO2, BT1, BT2, BT3 and BT4 samples.

conditions and the experimental data error was <1%.

3. Results and discussions

3.1. Characterizations

3.1.1. XRD

X-ray diffraction (XRD) was employed to determine the crystal phase of the as-synthesized Bi_2WO_6/TiO_2 samples. The XRD patterns of as-prepared samples are displayed in Fig. 2. The crystal structures of pure Bi_2WO_6 and single TiO_2 are also investigated for comparison with composite photocatalysts. The diffraction peaks of the single TiO_2 locating at $2\Theta = 25.3°,37.3°,47.6°,53.5°,55.1°$, and 62.2° are ascribed to (101), (004), (200), (105), (201) and (204) plans of anatase TiO_2 (JCPDS, No. 21–1272) [62]. The diffraction peaks of Bi_2WO_6 at $2\Theta = 28.29°$, 32.91°, 47.13°, 55.82°, 58.53°,68.7°, 75.92°, and 78.53° are related to the (131), (200), (202), (331), (262), (400), (193), and (402) crystal planes of the orthorhombic Bi_2WO_6 (JCPDS No. 39–0256) [30]. The peaks are sharp and no impurity was observed, indicating that Bi_2WO_6 was a pure phase with excellent crystallinity. There are no changes in characteristic diffraction peaks positions for anatase TiO_2 nanobelts and Bi_2WO_6 nanosheets in Bi_2WO_6/TiO_2 composite photocatalysts. No extra peaks were observed in heterostructure photocatalysts, indicating that Bi_2WO_6 and TiO_2 are successfully composited. Thus, the results attribute that the coupling of two photocatalysts did not influence on their crystal structure [63]. Both typical diffraction peaks of TiO_2 and Bi_2WO_6 phases are found in the Bi_2WO_6/TiO_2 composites and strong peaks in composites attribute to the high crystallinity of the heterojunctions. Thus, the XRD patterns confirm successful deposition of Bi_2WO_6 on TiO_2 nano-belts [64]. As shown in Fig. 3, after deposition of Bi_2WO_6 nanosheets on TiO_2, the characteristic peaks of TiO_2 in the TiO_2/Bi_2WO_6 become weak compared to the pure TiO_2 nanobelts. The peak intensity at 25.3° which is related to TiO_2 constantly decrease after loading Bi_2WO_6 on TiO_2. Moreover, the intensity of characteristic peaks of Bi_2WO_6 in composite photocatalysts gradually increases with increasing Bi_2WO_6 concentration.

3.1.2. DRS

The photocatalytic activity depends on the photo-absorption characteristics of photocatalysts which in turn mainly relates to the structure of energy bands. Fig. 3a shows UV–vis diffuse reflectance spectroscopy (DRS) of Bi_2WO_6, TiO_2 and Bi_2WO_6/TiO_2 composite samples. It can be seen that except for pure TiO_2, which can absorb only ultraviolet light (~385 nm), all other photocatalysts can absorb both UV and visible light. Among the as-prepared photocatalysts, the TiO_2 has the largest bandgap and displays UV light absorption ($\lambda < 400$ nm). These results are correspond to the optical properties of TiO_2 [30]. The light absorption range of Bi_2WO_6 is up to 400 nm and shows a relatively strong light absorption capacity in both the UV and visible light regions. The photo-absorption range of Bi_2WO_6 extends from the UV region to the visible region and that threshold of absorption wavelength can be seen at about 412 nm. The bandgap of Bi_2WO_6 photocatalyst is about 2.8 eV [40]. The light absorption capacity of composite photocatalysts enhance towards visible light after the introduction of Bi_2WO_6 to TiO_2 and shows a red shift. The results indicate the formation of heterojunction structure as a result of the change in energy band because of formation of composite between Bi_2WO_6 and TiO_2. The composite formation leads to the excellent electron migration in the interface contact of Bi_2WO_6 nanosheets and TiO_2 nanobelts [65–67]. Fig. 3b shows that the intensity of absorption of visible light increases with Bi_2WO_6 increment in the composites. Compared with pure TiO_2 which is only active under ultraviolet irradiation, Bi_2WO_6/TiO_2 composites are active in both

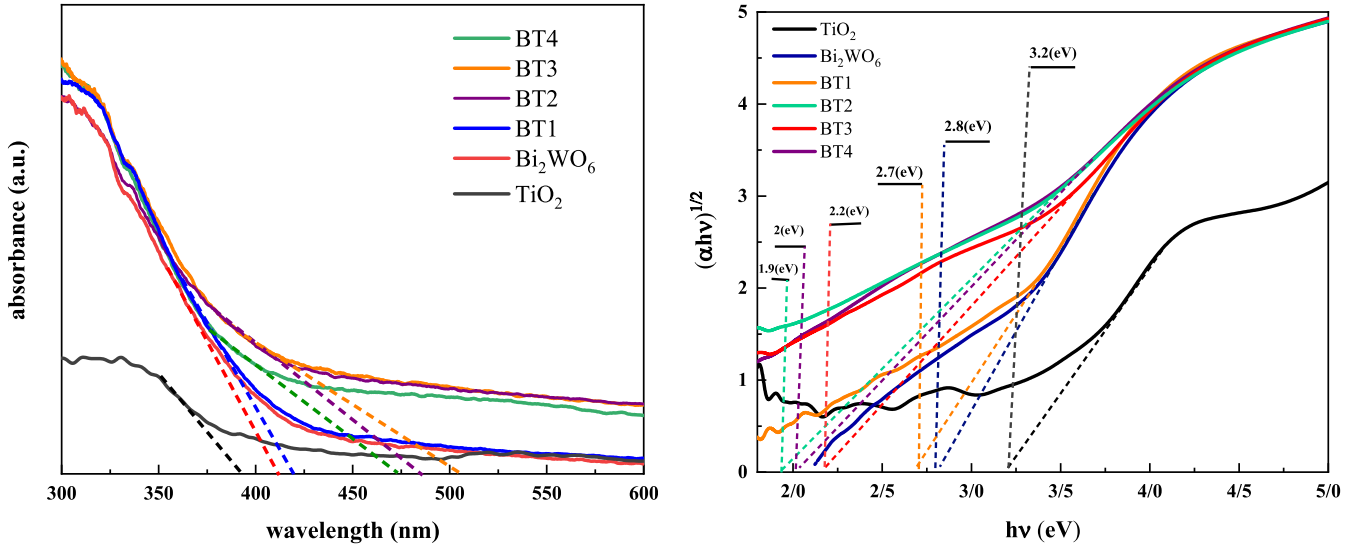

Fig. 3. a. UV–vis absorption spectra of Bi2WO6, TiO2, BT1, BT2, BT3 and BT4 samples.
b. Tauc plot of Bi2WO6, TiO2, BT1, BT2, BT3 and BT4 photo-catalysts.

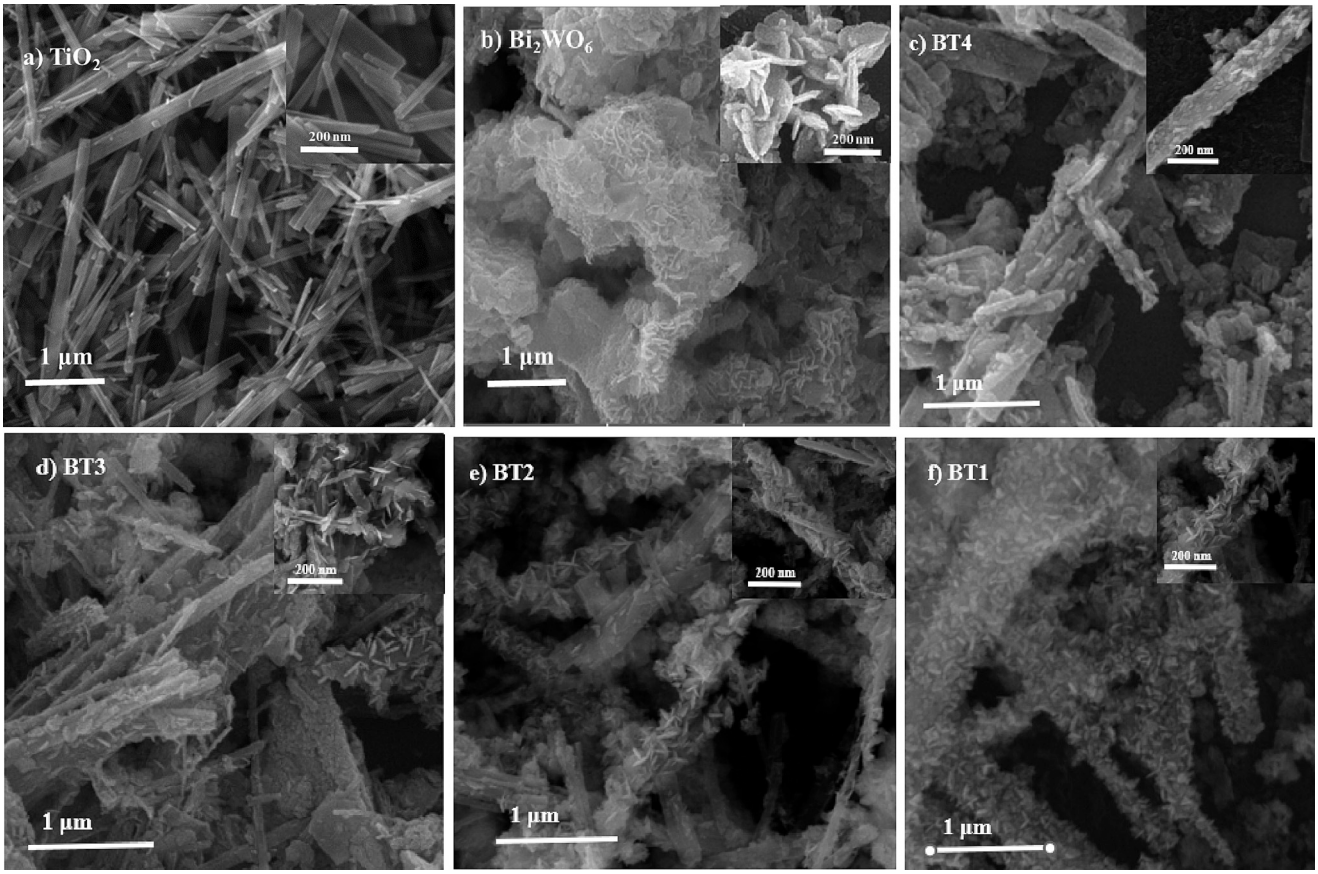

Fig. 4. FESEM images of photo-catalysts: (a) TiO_2 and (b) Bi_2WO_6 (c) BT4, (d) BT3, (e) BT2 and (f) BT1.

ultraviolet and visible region due to the synergistic effect of Bi_2WO_6 and TiO_2. The absorption edges of the Bi_2WO_6/TiO_2 photocatalysts change with different Bi_2WO_4 nanosheets loading.

The photocatalyst photo-absorption capacity explains by the bandgap using the Tauc-plot. The bandgap can be calculated according to the Kubelka–Munk (K-M) equation as follows:

$$Ahv = A\left(hv - E_{bg}\right)^{n/2} \quad (2)$$

Where α, h, v, E_g, and A respectively are the coefficient of absorption, Planck constant, frequency of light, the semiconductor bandgap, and a constant of proportionality. The n value depends on the nature of the semiconductor bandgap and photocatalyst transition type. The $n = 1$ is related to direct transition, while $n = 4$ is correspond to indirect transition. TiO_2 and Bi_2WO_6 are direct bandgap semiconductors. Thus, the n value is 1 for anatase TiO_2 and Bi_2WO_6 semiconductors [68,69].

The addition of Bi_2WO_6 affects the absorption wavelength thresholds and the bandgap values of Bi_2WO_6/TiO_2 photocatalyst. The bandgaps of the TiO_2 and Bi_2WO_6 are about 3.2 and 2.8 eV, respectively. The band gap width of the different photocatalysts was in the order of: $TiO_2 > Bi_2WO_6 > Bi_2WO_6/TiO_2$. The band gap energies of BT1, BT2, BT3 and BT4 are calculated to be 2.7, 1.9, 2.2 and 2 eV, respectively. Bi_2WO_6/TiO_2 photocatalysts with different molar ratio of Bi_2WO_6 to TiO_2 have different bandgaps. The absorption band edge of the Bi_2WO_6/TiO_2 composites displays different degrees of redshift. This results are attribute to the formation of heterojunction structure [63]. The bandgap values of composite photocatalysts decrease with increasing Bi_2WO_6 loading on TiO_2 nanobelts up to BT2. The BT1 sample has higher bandgap value than BT4, BT3 and BT1 samples. At higher Bi_2WO_6 concentration, Bi can act as the recombination centers of electron-holes carriers [21]. BT2 has the highest absorption- wavelength threshold, which is correspond to the smallest Eg (1.9 eV). Therefore, the BT2 photocatalyst is predicted to have the optimal photocatalytic performance in the visible light region, because increasing in the utilization of light energy leads to improve the photocatalytic activity.

3.1.3. FESEM and EDX

The morphological properties of Bi_2WO_6, TiO_2 and Bi_2WO_6/TiO_2 samples were shows in Fig. 4. TiO_2 has a thin and long 1D structure with a narrow diameter ranging below 100 nm. The bare Bi_2WO_6 shows a 3D flower-like structure. The 2D nanosheets grown in all directions constructed the Bi_2WO_6 3D flower-like structure. TiO_2 nanobelts have a rough surface that provides nucleation spots for assembling Bi_2WO_6 nanosheets. The two-dimensional Bi_2WO_6 nanosheets are deposited on the surface of each TiO_2 nanobelt. With the increase of the Bi_2WO_6 to TiO_2 molar ratio, more Bi_2WO_6 nanosheets are deposited on the TiO_2 nanobelts. The size and density of Bi_2WO_6 nanosheets increase with increase of Bi_2WO_6 content, which is correspond with increase in peak intensity of Bi_2WO_6/TiO_2 samples in XRD patterns. With increasing the deposition amounts of Bi_2WO_6, 2D Bi_2WO_6 nanosheets uniformly are connected and loaded on the TiO_2 nanobelts, which constructed the three-dimensional networks composite. The nano-sheets structure of Bi_2WO_6 provides a higher specific surface area than nanoparticles. The uniform distribution of Bi_2WO_6 nanosheets over TiO_2 nanobelts observes in Fig. 4. Thus, a good interaction of Bi_2WO_6 with TiO_2 nanobelts was achieved, which would benefit heterojunction development with a higher transition of electrons.

The TEM image and corresponding elemental mapping of BT2 sample is shown in Fig. 5. The results exhibit uniform dispersion of Bi_2WO_6 nanosheets on TiO_2 nanobelts with nanometric size, where the nanosheets homogenously coating the nanobelts. Moreover, loading the Bi_2WO_6 nanosheets does not affect the TiO_2 nanobelt structure. The EDX analysis also demonstrates that the BT2 sample contains Ti, Bi, W, and O

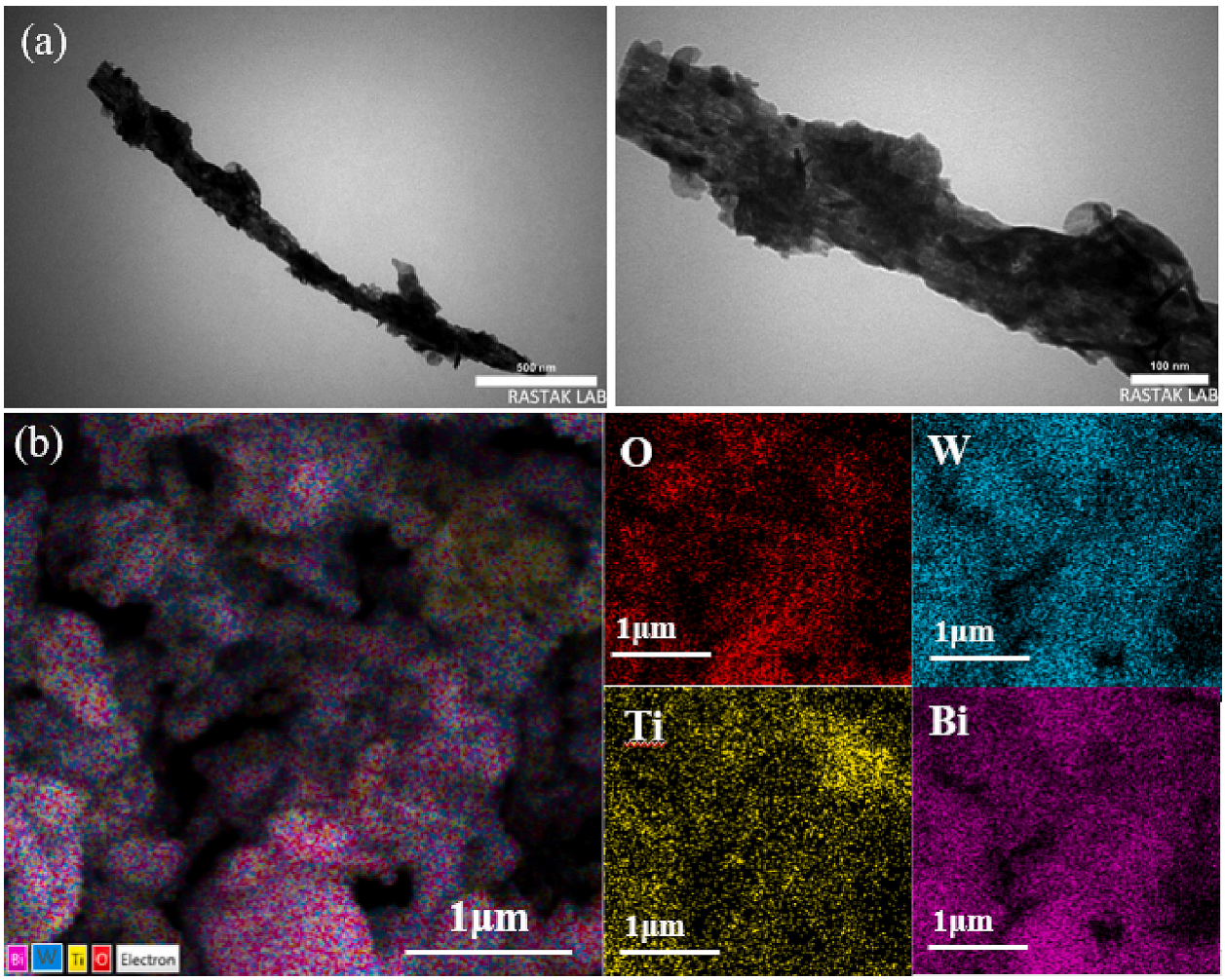

Fig. 5. (a) TEM and (b) Elemental mapping analysis of BT2 sample.

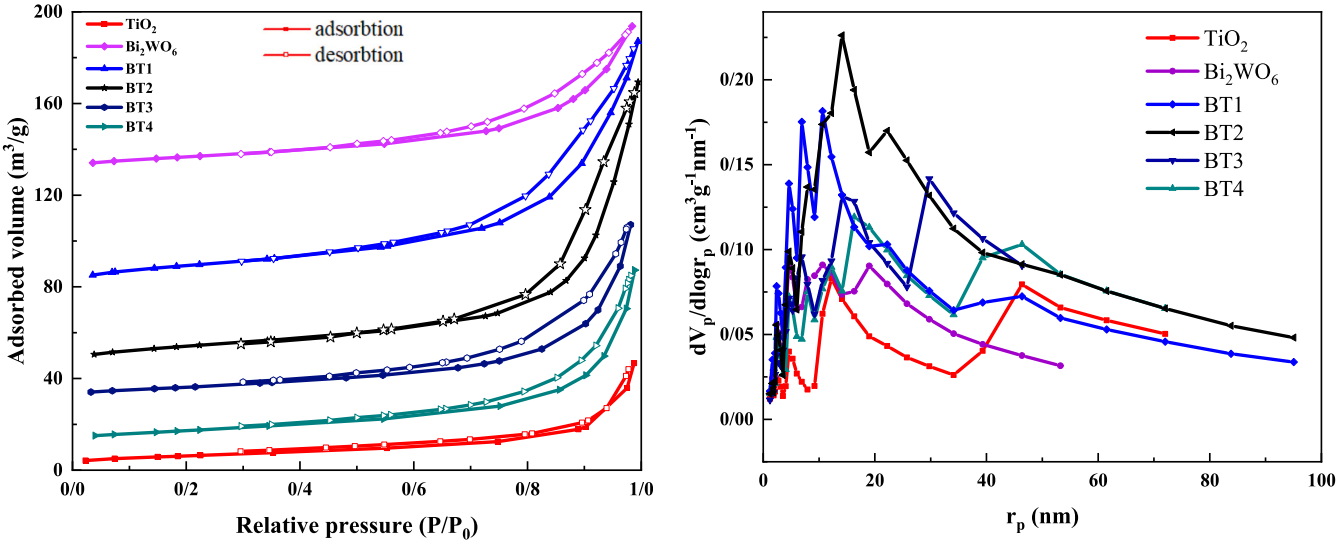

Fig. 6. a. N_2 adsorbtion–desorption isotherms for catalyst samples.
b. Pore size distribution of samples.

atoms (Fig. S2). These results show the coexistence of TiO_2 and Bi_2WO_6 in this sample. It is known that the interface connection between two substances of the composites significantly affects migration performance of photo-generated charge carriers [64,67]. Thus, interface connection of BT2 composites ingredients would be favour for transformation and separation of photo-induced charge carriers which in turn enhances the

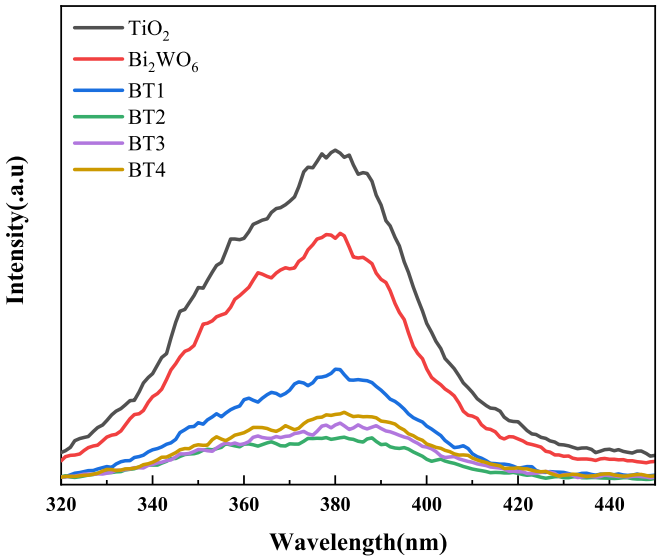

Fig. 7. Photoluminescence spectra of synthesized photocatalysts.

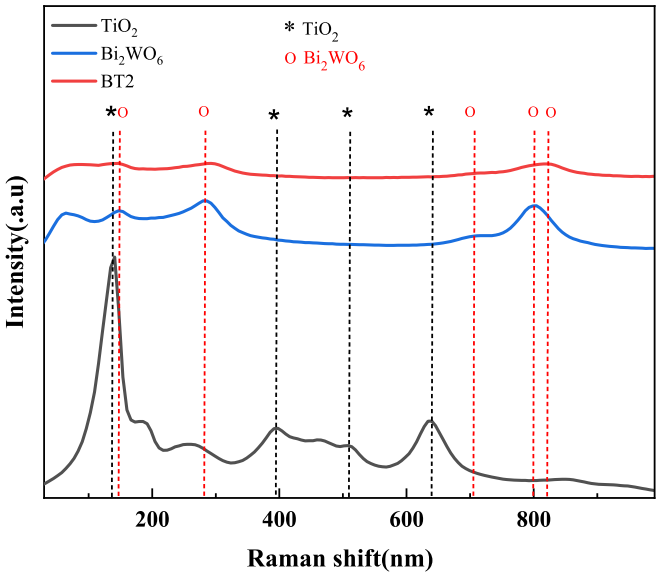

Fig. 8. Raman spectra of TiO_2, Bi_2WO_6 and BT2.

Table 1
Physiochemical properties of photo-catalysts.

Photocatalyst	BET surface area (m^2/g)	Pore volume (cm^3/g)	Average pore diameter (nm)	Band gap (eV)	CH_4 yield (μmol. g^{-1}. h^{-1})	AQY (%)
TiO_2	21.83	0.072	13.24	3.2	0.51	0.013
Bi_2WO_6	30.97	0.101	13.07	2.8	1.01	0.023
BT1	40.40	0.162	16.12	2.7	1.4	0.036
BT2	36.84	0.186	19.68	1.9	2.37	0.062
BT3	29.99	0.122	16.35	2.2	1.74	0.045
BT4	29.71	0.121	16.27	2.0	1.53	0.040

photocatalytic performance. The high adsorption capacity of reactant molecules on photocatalysts is the primary and critical step in CO_2 photocatalytic conversion reaction and can influence the photocatalytic activity and selectivity. The nanosheet structure on TiO_2 nanobelts are suggested to provide more sites for adsorption of carbon dioxide and other reactant molecules [40].

3.1.4. N_2 physisorption

The isotherms curve of N_2 adsorption–desorption of as-prepared TiO_2, Bi_2WO_6, and Bi_2WO_6/TiO_2 samples are presented in Fig. 6a. Furthermore, the pore size distribution (BJH) of the TiO_2, Bi_2WO_6, and Bi_2WO_6/TiO_2 photocatalysts is displayed in Fig. 6b. All isotherms exhibit a larger desorption volume than the related absorption volume. The hysteresis loops are observed in the relative pressure range of 0.3–1.0. These isotherms are in agreement with type IV curve and the H3 hysteresis loop, based on the IUPAC classification which can be attributed to the presence of slit-shaped mesopore structure for all samples [70,71]. The results are in agreement with the morphological properties of samples according to the FESEM images. According to the pore-size distribution curves of Fig. 7b, the average pore diameter of TiO_2, Bi_2WO_6, and Bi_2WO_6/TiO_2 samples are in the range of 13–20 nm.

The surface area, pore volume, and pore-structure parameters of as-prepared photocatalysts are summarized in Table 1. The surface area of TiO_2, Bi_2WO_6 and Bi_2WO_6/TiO_2 photocatalysts enhance in the following order: BT1 > BT2 > BT3 > BT4 > Bi_2WO_6 > TiO_2, which means that Bi_2WO_6 nanosheets loading on TiO_2 enhances the specific surface area. This results are in agreement with previous works that surface area of Bi_2WO_6/TiO_2 composites sample increases with increasing the concentration of Bi_2WO_6 on TiO_2 [39,72,73]. After the composite formation, the specific surface area of all Bi_2WO_6/TiO_2 samples increase from 29.71 to 40.40 m^2/g. The increasing in the specific surface area of composites indicates increasing efficiency of contact between the surface of photocatalyst and reactant molecules, which can facilitate the adsorption capacity of reactant molecules and enhance their photoreduction performance. As shown in Table 1, deposition of Bi_2WO_6 nanosheets on TiO_2 increases the pore diameter from 16.12 to 19.68 nm. A large surface area and pore size can increase the contact chance of photocatalyst with reactants [62,63].

3.1.5. PL

The releasing energy from recombination of electron−hole carriers can be explain by photo- luminescence emission. Typically, the weaker PL intensity is attributed to low recombination rate of electron−hole pairs, which leads to enhanced photocatalytic performance [68]. The photoluminescence (PL) spectra were carried out with 290 nm excitation wavelength to investigate the photo-carriers migration and recombination behaviours. Fig. 7 shows the PL spectra of synthesized TiO_2, Bi_2WO_6, and Bi_2WO_6/TiO_2 photocatalysts in 320–450 nm. The spectra of all photocatalysts have a peak at around 380 nm wavelength. The photo-luminescence spectra decrease in the order of TiO_2 > Bi_2WO_6 > Bi_2WO_6/TiO_2. The results exhibit that the deposition of Bi_2WO_6 nanosheets on TiO_2 nanobelts can improve the separation of photo-generated charge carriers. It is clear that the photo-luminescence intensity of Bi_2WO_6/TiO_2 samples are lower than pure Bi_2WO_6 and TiO_2. The PL spectra intensity of the BT1 sample is lower than that of TiO_2 nanobelts that is attributed to the easy photo-generated charge carriers migration between TiO_2 and Bi_2WO_6 in the composite photocatalysts. The PL spectra of Bi_2WO_6/TiO_2 samples with the lower intensity than pure TiO_2 and Bi_2WO_6 illustrate that the photo-induced carriers can transfer easily between the interface of Bi_2WO_6 and TiO_2 and thus, the recombination rate of carriers decrease in the Bi_2WO_6/TiO_2 samples, which is in accordance with their photocatalytic activity. The intensity of Bi_2WO_6/TiO_2 composite signals decrease with increase of Bi2WO6 deposition up to BT2. The BT1 photocatalyst shows higher PL intensity compared to BT2, BT3 and BT4 possibly due to formation of new recombination centers by excessive Bi_2WO_6 nanosheets [22]. The BT2 composite exhibit the lowest PL emission intensity among all of the as-prepared photocatalysts, which is attribute to the slowest charge recombination rate of this photocatalyst [39].

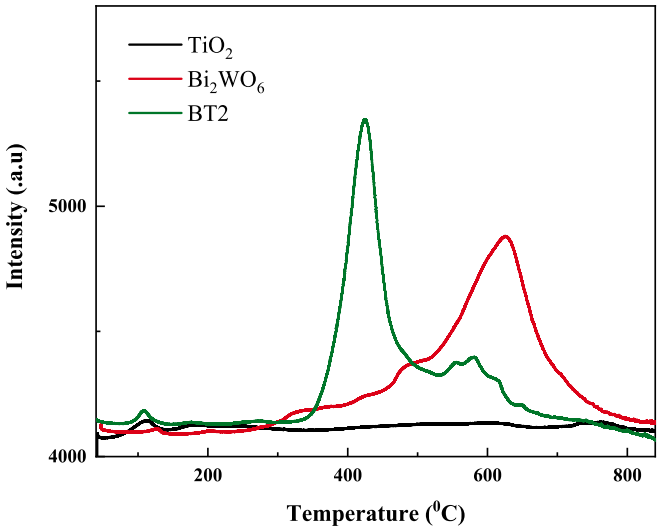

Fig. 9. CO_2-TPD results of TiO_2, Bi_2WO_6 and BT2 from 30 to 850 °C.

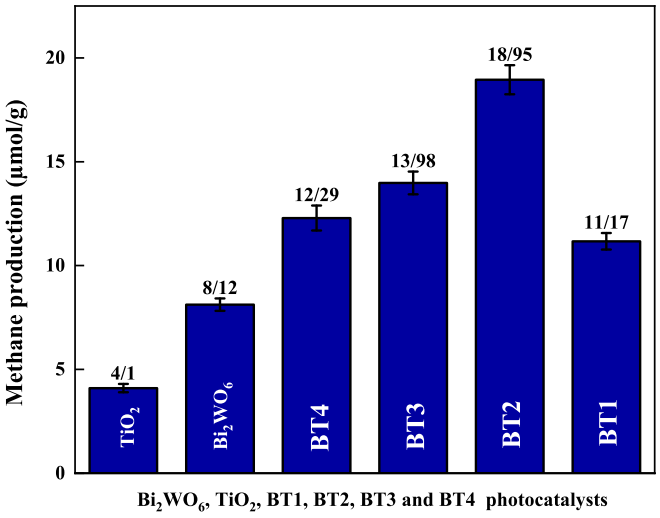

Fig. 10. CH_4 yield over different photo-catalysts after 8 h of reaction.

3.1.6. *Raman analysis*

Fig. 8 shows Raman spectra of TiO_2 nanobelt, Bi_2WO_6 nanosheet, and BT2 photocatalysts. The typical vibrational bands of the anatase phase of TiO_2 at 141, 398, 516, 633 cm^{-1} are according to the Eg(1), B1g (1), A1g + B1g(2), and Eg(2) modes, respectively [13,73]. The Raman shifts at 141 and 633 cm^{-1} are related to the of O–Ti–O symmetric bending. The Raman peaks at 398 and 516 cm^{-1} are correspond to O–Ti–O symmetric stretching and counter-bending vibrations [74]. The typical vibrational bands at 149, 280, 718,797, and 830 cm^{-1} are related to A2u, A1g, Eu, Eu, and Eg orthorhombic Bi_2WO_6 vibration mode [40,75]. The peak at 148 cm^{-1} is correspond to the WO_6 octahedron external vibration mode. The peak at 280 cm^{-1} is attributed to the f Bi—O vibrations bond [66]. The peak located at 718 cm^{-1} is attributed to the asymmetric vibration bending W—O. The peaks positioned at 797 and 830 cm^{-1} are signatures of bismuth tungstate. These peaks are corresponds to the antisymmetric and symmetric modes of terminal O-W-O, respectively [76].

The Raman spectrum of BT2 shows absorption peaks at 145, 295, 728, and 808 cm^{-1}. The results show that the loading of Bi_2WO_6 nanosheets on TiO_2 affects the Raman peak intensity of TiO_2 in BT2 sample. No evidence of TiO_2 anatase bands can be observed and just the characteristic Raman peaks of Bi_2WO_6 appear in the Raman spectra of BT2 composite photocatalyst. Comparing absorption peak position of BT2 photocatalyst with pure Bi_2WO_6 exhibits a slightly shift to the right that can explain by the formation of interfacial interactions between Bi_2WO_6 nanosheets and TiO_2 nanobelts, which results in a change in the interface tension and lattice stress. This may suggests that the formation of BT2 photocatalyst inhibits the TiO_2 and Bi_2WO_6 vibrations [76,77].

3.1.7. *CO_2- TPD*

The adsorption step is a first and vital step of carbon dioxide photocatalytic reduction which is typically performed at the interface between photocatalyst and CO_2 molecules in the gas phase. The CO_2 temperature-programmed desorption (TPD) analysis were applied to investigate the CO_2 adsorption efficiency of photocatalysts. The adsorption property of photocatalyst is attributed to the photocatalytic activity of CO_2 photoreduction reaction. Commonly, desorption peak area and temperature are related to CO_2 adsorption capacity of photocatalysts. The area of desorption peak is proportional to the number of the active sites on the photocatalyst surface, while the temperature of desorption peak is related to the adsorption strength of species on the active sites. Typically the weak, medium and strong active sites are attributed to the desorption temperature range from 100 to 300 °C, 300–450 °C and 450–600 °C, respectively [78]. Fig. 9 shows the CO_2 temperature-programmed desorption (TPD) analysis of Bi_2WO_6, TiO_2 and, BT2 photocatalysts. The single TiO_2 shows two peaks at 110 °C and 760 °C that is explained the weak and strong types of interactions between carbon dioxide molecules and the surface of the TiO_2 photocatalyst, respectively. The weak CO_2 desorption peak below 150 °C observed for Bi_2WO_6 is attributed to the weak absorption of CO_2 [41]. The profile of Bi_2WO_6 displays two moderate peaks at 320 °C and 430 °C and two strong peaks at 500 °C and 640 °C that are attributed to the moderate and a high strength of CO_2 adsorption. The BT2 composite photocatalyst displays desorption peak with higher intensity compared to the pure TiO_2 and Bi_2WO_6 samples. The high CO_2 desorption amount of composite photocatalyst is related to the adsorption of the higher number of CO_2 molecules on the surface of photocatalysts which can further participate in photoconversion reaction and lead to the improved photocatalytic performance. The BT2 composite exhibits an intensive peak at 300–500 °C that is according to a medium or strong CO_2 adsorption. The results suggest the excellent CO_2 adsorption characteristic of the BT2 composite photocatalyst. The intensity of the peak observed at 300–500 °C is higher for BT2 composite compared to Bi_2WO_6 photocatalyst suggests that more CO_2 adsorb over BT2 than Bi_2WO_6 in moderate strength area, which can be considered as a reason for high photocatalytic activity of BT2 composite observed.

3.2. *CO_2 photo-reduction activity*

CO_2 photocatalytic reduction was carried out in the gas phase closed photoreactor at ambient pressure and low temperature (40 °C) under UV- vis light irradiation of a Hg lamp (250 W, > 350 nm). A number of experiments were performed under several control conditions: (1) in the absence of light illumination on the samples, (2) in the absence of CO_2 gas flow (under Ar atmosphere), (3) in the absence of photo-catalyst and (4) in the absence of H_2O. No detectable amount of hydrocarbons in blank test indicate that methane is only produced from CO_2 though photocatalytic reduction reaction with H_2O [22]. Fig. 10 shows the methane production yield over all samples after 8 h of reaction under UV–vis light illumination. The methane production of TiO_2 photocatalyst after 8 h is about 4.1 µmol/g. The results exhibit that the TiO_2, Bi_2WO_6 and composites photocatalytic activity varies in the order of: BT2 > BT3 > BT4 > Bi_2WO_6/TiO_2 > Bi_2WO_6 > TiO_2. Deposition of Bi_2WO_6 nanosheets on TiO_2 nanobelts results in an increase in the CO_2 production yield. The excellent performance of Bi_2WO_6/TiO_2 photocatalysts might be a result of the low recombination rate of photoinduced electron-hole pairs and simultaneous charge carries migration between TiO_2 and Bi_2WO_6. The synergistic effect of the addition of

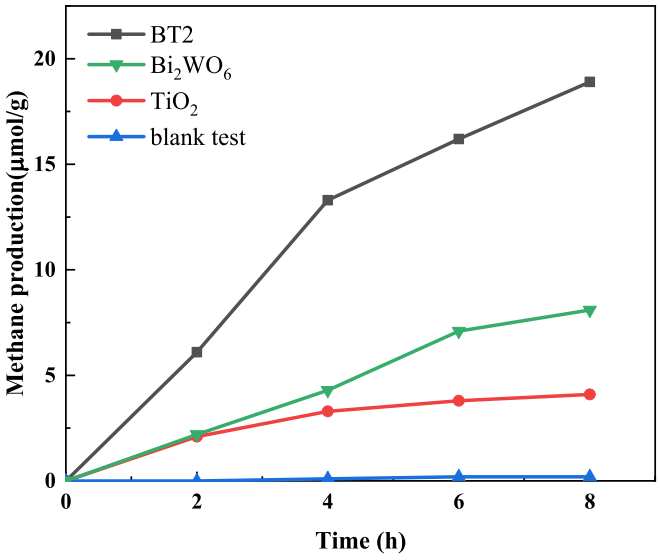

Fig. 11. Time-on-line CH_4 yield over different samples during 8 h of reaction.

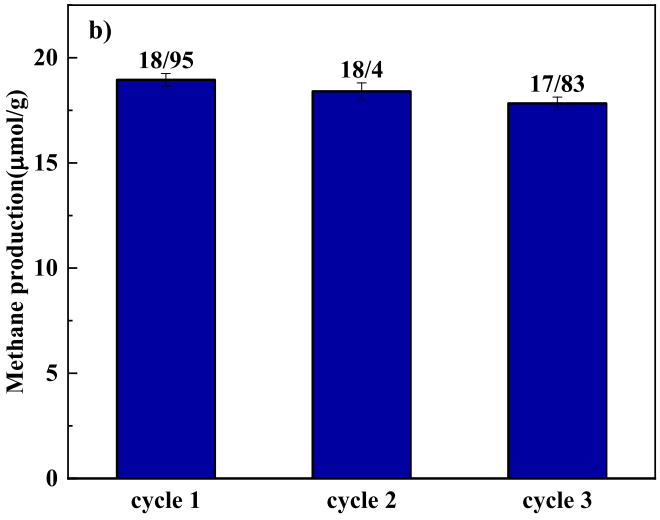

Fig. 12. Stability of BT2 photocatalyst during 3 reaction cycles.

Bi_2WO_6 nanosheets on TiO_2 nanobelts leads to an increase in the lifetime of electron-hole pairs. Thus, it can improve the photocatalytic performance of the composite photocatalysts. The results show that the photocatalytic performance of TiO_2 can develop after the introduction of Bi_2WO_6 on TiO_2. The methane evolution is enhanced by increasing the deposition amount of Bi_2WO_6 nanosheets in composites. At the optimal loading (BT2 photocatalyst) total CH_4 yield was 18.95 μmol/g, which is higher than that of the pure TiO_2 and Bi_2WO_6 samples. The maximum AQY of methane production was 0.28% for BT sample, which is about 5 times higher than that of pure TiO_2 sample (Table 1). It can explain by the formation of heterojunction between the TiO_2 nanobelts and Bi_2WO_6 nanosheets interfaces. Nevertheless, when the Bi_2WO_6 content in Bi_2WO_6/TiO_2 composite is enhanced beyond its optimal amount, a decrease in CH_4 production can be seen, suggesting the excess Bi_2WO_6 amount may cover the TiO_2 surface or be self-agglomerate. Therefore, the deposition amount of Bi_2WO_6 nanosheets on TiO_2 nanobelts surface plays an important role in photoreduction activity of Bi_2WO_6/TiO_2 heterojunctions. The CH_4 production is well consistent with the DRS, PL and TPD-CO_2 analyses results. In brief, loading Bi_2WO_6 on TiO_2 enhances the optical properties by increasing the visible light absorption efficiency and decreasing bandgap. Thus, BT2 sample can absorb the highest visible light among the composite samples, limit charge carrier recombination, and absorb more reactant molecules. Therefore, the methane production can enhance for composite photocatalysts compared with single TiO_2. The BT2 photocatalyst is optimal photocatalyst with Bi_2WO_6 to TiO_2 molar ratio of ½. However, further loading than optimal contact leads to a decrease in methane production yield due to the possible formation of the additional electron-hole carriers recombination centres or limited absorption light efficiency in presence of excess Bi_2WO_6 that cover the TiO_2 surface. The photocatalytic performance towards the photoreduction of CO_2 was also investigated as a function of irradiation time from 0 to 8 h (Fig. 11). CH_4 generation occurred after irradiation and the methane production increase with irradiation time increment in the presence of TiO_2, Bi_2WO_6 and BT2 catalysts. The methane production over BT2 is higher than methane production over TiO_2 and Bi_2WO_6 samples. The stability of BT2 catalyst towards photocatalytic conversion of CO_2 to methane is shown in Fig. 12. The BT2 catalyst shows a subtle decrease (<5%) in methane production during three runs.

The valence band and conduction band potential of TiO_2 and Bi_2WO_6 semiconductors can be calculated by $E_{CB} = X - E_0 - 0.5E_g$ and $E_{VB} = E_{CB} + E_g$ [79], where E_{VB} and E_{CB} are valence band energy and conduction band potential energy, E_g reflects the semiconductor's band gap energy (3.2 eV and 2.8 eV for TiO_2 and Bi_2WO_6,respectively), X represents absolute electronegativity of atoms in semiconductors (5.81 and 6.36 for

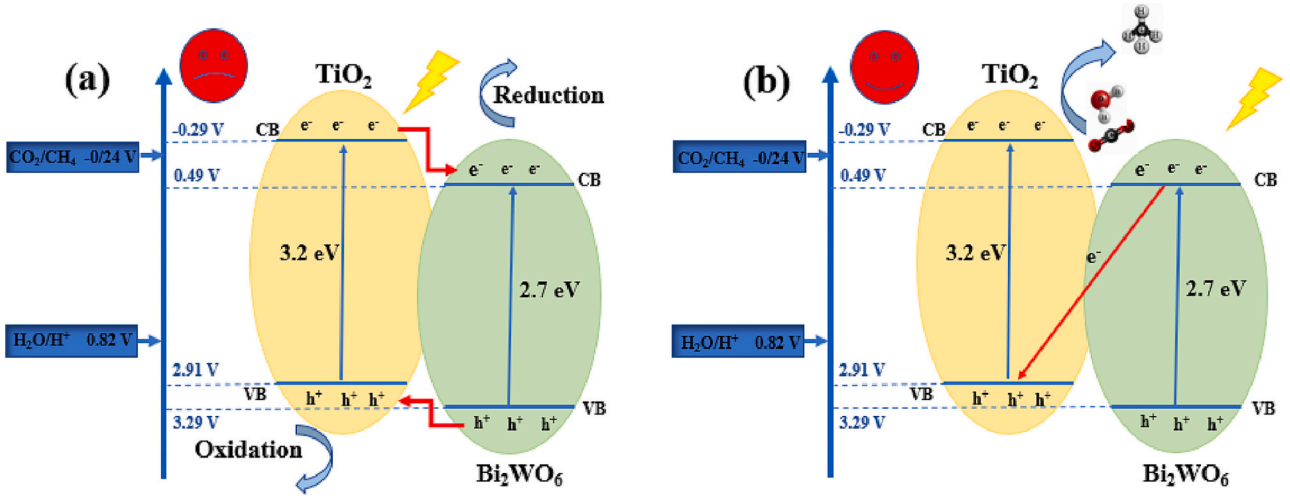

Fig. 13. (a) Double-charge transfer mechanism (b) and *Z*-scheme mechanism of CO_2 photoreduction over Bi_2WO_6/TiO_2 catalyst.

TiO_2 and Bi_2WO_6 [62], respectively), E_0 is free electrons potential energy on hydrogen scale, which is equal to 4.5 eV [63]. Therefore, the valence band of TiO_2 and Bi_2WO_6 are calculated as 2.91 eV and 3.29 eV, respectively, while related conduction band are −0.29 eV and 0.49 eV, respectively. According to matchable energy band between Bi_2WO_6 and TiO_2, both conventional type II and direct *Z*-scheme heterojunction mechanism are proposed. The scheme of either double-charge transfer and Z-scheme transfer possible mechanism of Bi_2WO_6/TiO_2 composite exhibit in Fig. 13. When Bi_2WO_6 and TiO_2 come into contact, a heterojunction structure is formed. After irradiation, photoexcited charge carriers are generated in both TiO_2 and Bi_2WO_6 semiconductors. If charge migration routes of Bi_2WO_6/TiO_2 composite follow the conventional type II mechanism (Fig. 13a), since the conduction band edge of TiO_2 nanobelt is 0.78 eV higher than that of Bi_2WO_6 nanosheet, the photoexcited electron of TiO_2 can migrate to conduction band of Bi_2WO_6. The valence band level of Bi_2WO_6 is 0.38 eV lower than that of TiO_2, the holes on valence band of Bi_2WO_6 can transfer to TiO_2 [80]. The photoinduced electrons diffuse from TiO_2 nanobelts to Bi_2WO_6 nanosheets while holes diffuse from Bi_2WO_6 to TiO_2. Thus, negative charges accumulate at Bi_2WO_6 and positive charges gather at TiO_2 [75]. Formation of heterojunction moves up the Fermi level of TiO_2 and Bi_2WO_6 Fermi level shifts downward until matching the Fermi levels energy, which generates an internal electric field at interface of two semiconductors [63]. The internal electric field close to heterointerface may leads to rapid and direct migration of electrons in TiO_2 to Bi_2WO_6 and holes in Bi_2WO_6 to TiO_2 [54,81]. This charge carries migration and formation of heterojunction can enhance the electron-holes separation efficiency. The potential for photocatalytic reduction of CO_2 to methane and CO is −0.24 V and − 0.53 V, respectively [48]. The potential for oxidation of water is 0.82 V [82]. The concentrate electrons in conduction band of Bi_2WO_6 are not able to CO_2 reduction to methane because the conduction band of Bi_2WO_6 (0.49 eV) is more positive than redox potential of CO_2/CH_4 (−0.24 V). Thus, the possible reaction mechanism can be as follow the *Z*-scheme charge transfer mechanism [83]. As shown in Fig. 13b, Electrons in TiO_2 and Bi_2WO_6 valence band are excited to conduction band due to light absorption and the same number of holes are generated in valence band of TiO_2 and Bi_2WO_6. The portion of photoexcited electron on CB of Bi_2WO_6 can migrate to valence band of TiO_2 phase and subsequently electrons excited to conduction band of TiO_2. Thus, formation of heterojunction composite inhibits electron-holes recombination. Combination of electron from conduction band of Bi_2WO_6 and holes from valence band of TiO_2 leads to provide more effective holes on valence band of Bi_2WO_6 for water oxidation reaction, which provides more H^+ to methane production as major product [84]. The electrons on TiO_2 conduction band have enough reduction ability to CO_2 reduction to methane. The photoexcited electrons on TiO_2 can participate in CO_2 reduction reaction. The CO_2 molecules can absorb on catalyst surface. The absorbed CO_2 molecules can be converted to methane by multielectron transfer process. The possible mechanism of CO_2 photoreduction over Bi_2WO_6/TiO_2 composite can be proposed according to characteristic properties and photocatalytic performance of samples. Formation of heterojunction between Bi_2WO_6 nanosheets and TiO_2 nanobelts accounts for excellent photocatalytic activity. The primary steps of CO_2 photocatalytic reduction process involve: (1) light absorbtion, (2) generation and migration of photoexcited charge carriers, (3) absorption of CO_2 molecules and activation through accepting photoinduced electrons. The nanoscale and electronic structure of Bi_2WO_6/TiO_2 composite leads to improve the above-mentioned steps. Deposition of Bi_2WO_6 on TiO_2 leads the enhancement of visible light absorption efficiency. According to TPD-CO_2 analysis, loading Bi_2WO_6 on TiO_2 can enhance CO_2 absorption efficiency to participate in CO_2 reduction reaction. Besides, a built-in a heterojunction between two semiconductors in composite sample provide interfacial charge channel to accelerate electron migration. Thus, a heterojunction formation between Bi_2WO_6 and TiO_2 accelerate direct transformation and separation of photoinduced charge carriers. The

Table 2
Products yield of CO_2 reduction using Bi_2WO_6–containing photocatalyst.

Photocatalyst	Product yield ($\mu mol/g_{cat}.h$)	Experimental Condition: Reactants, Reactor type, Light source, Temperature (°C) and Pressure (atm)	Reference
TiO_2	0.33(μmol/g.h) CH_4	CO_2 gas with H_2O, gas-phase batch, 250 W (Hg lamp), 25 °C and 1 atm	[21]
Bi_2WO_6 nanosheets	0.63(μmol/g.h) CH_4 7.12(μmol/g.h) CO	CO_2 gas with H_2O, gas-phase batch, 300 W (Xe lamp), 25 °C and 1 atm	[85]
Bi_2WO_6	0.15(μmol/g.h) CH_4 2.37(μmol/g.h) CO	CO_2 gas with H_2O, gas-phase continues flow, OmniCure S2000 UV–vis lamp (250–600 nm), 25 °C and 1 atm	[86]
Bi_2WO_6	0.01(μmol/g.h) CH_4 1.17(μmol/g.h) CO	CO_2 gas with H_2O, gas-phase continues flow, UV–vis lamp, 25 °C and 1 atm	[40]
Bi_2WO_6	0.37(μmol/g.h) CH_4 7.7(μmol/g.h) CO	CO_2 gas with H_2O, gas-phase batch, UV − vis light (Perfect-light, PLS-SXE300D, 380 nm),25 °C and 1 atm	[87]
Bi_2WO_6 nanosheets	1.01(μmol/g.h) CH_4	CO_2 gas with H_2O, gas-phase batch, 300 W (Xe lamp), 25 °C and 1 atm	[88]
Bi_2WO_6 square nanoplate	1(μmol/g.h) CH_4	CO_2 gas with H_2O, gas-phase batch, 300 W xenon arc lamp, (λ > 420 nm), 25 °C and 1 atm	[89]
Bi_2WO_6-Oxygen vacancy	1.67(μmol/g.h) CH_4	CO_2 gas with H_2O, gas-phase batch, Simulated solar light, 25 °C and 1 atm	[90]
Cl- Bi_2WO_6	1.65(μmol/g.h) CH_4 0.16(μmol/g.h) CO	CO_2 gas with H_2O, gas-phase batch, 300 W Xenon lamp (PLS-SXE300, Beijing Perfect-light Co), 25 °C and 1 atm	[91]
Bi_2WO_6-TiO_2 binanosheets	0.7(μmol/g.h) CH_4 2.6(μmol/g.h) CO	CO_2 gas with H_2O, gas-phase batch, 300 W Xe lamp, 25 °C and 1 atm	[84]
BiWO-Ti	1.3(μmol/g.h) CH_4	CO_2 gas with H_2O, gas-phase fluidized bed, UV-LED lamp (365 nm), 25 °C and 1 atm	[92]
Ti_3C_2/Bi_2WO_6	1.78 (μmol/g.h) CH_4 0.44(μmol/g.h) CH_3OH	CO_2 gas with H_2O, liquid-phase batch 0.084 g $NaHCO_3$, 0.3 mL H_2SO_4 (2 mol/L), Xe lamp, Simulated sunlight irradiation, 25 °C and 1 atm	[93]
PtO_x/ Bi_2WO_6	18(ppm/g.h) CH_4	CO_2 gas with H_2O, gas-phase batch, 500 W Xe lamp, 25 °C and 1 atm	[94]
Bi_2WO_6 /BiOI	2.29(μmol/g.h) CH_4	500 W Xenon arc lamp (CHF-XM-500 W) equipped with an UV cut-off filter (to remove λ < 400 nm) was, continues reactor	[95]
Bi_2O_3/ Bi_2WO_6	1.5(μmol/g.h) CH_4 8(μmol/g.h) CO	CO_2 gas with H_2O, gas-phase batch, 300 WXe lamp with a cutofffilter (λ > 400 nm), 25 °C and 1 atm	[96]
Bi_2WO_6/WO_3	2.57 (μmol/g.h) CH_4	CO_2 gas with H_2O, gas-phase batch, 300 W Xe lamp, 40 °C and 1 atm	[97]
Bi_2WO_6/Cu/WO_3	1.1(μmol/g.h) CH_4	CO_2 gas with H_2O, gas-phase batch, 500 W Xenon arc lamp (CHF-XM-500 W), (λ > 400 nm), 25 °C and 1 atm	[98]
Bi_2WO_6/Au/CdS	1.52(μmol/g.h) CH_4	CO_2 gas with H_2O, gas-phase batch, 300 W Xe lamp, 25 °C and 1 atm	[99]
Bi_2WO_6/RGO/g-C_3N_4	2.2(μmol/g.h) CH_4 15.96(μmol/g.h) CO	CO_2 gas with H_2O, gas-phase batch, 300 W Xe lamp ((λ > 400 nm), 25 °C and 1 atm	[2]

(*continued on next page*)

Table 2 (*continued*)

Photocatalyst	Product yield (μmol/g_{cat}.h)	Experimental Condition: Reactants, Reactor type, Light source, Temperature (°C) and Pressure (atm)	Reference
CQDs- Bi_2WO_6	0.9 (μmol/g.h) CH_4	CO_2 gas with H_2O, gas-phase batch, 500 W Xe lamp (420 cutoff filter), 40 °C and 1 atm	[100]
BT1	1.4(μmol/g.h) CH_4	CO_2 gas with H_2O, gas-phase batch, 250 W (Hg lamp), 40 °C and 1 atm	This work
BT2	2.37(μmol/g.h) CH_4	CO_2 gas with H_2O, gas-phase batch, 250 W (Hg lamp), 40 °C and 1 atm	This work
BT3	1.74(μmol/g.h) CH_4	CO_2 gas with H_2O, gas-phase batch, 250 W (Hg lamp), 40 °C and 1 atm	This work
BT4	1.53(μmol/g.h) CH_4	CO_2 gas with H_2O, gas-phase batch, 250 W (Hg lamp), 40 °C and 1 atm	This work

possible mechanism can be ascribed according to following equations:

$$Bi_2WO_6 + h\nu \rightarrow Bi_2WO_6\ (h^+ + e^-)$$

$$TiO_2 + h\nu \rightarrow TiO_2\ (h^+ + e^-)$$

$$TiO_2 + Bi_2WO_6\ (e^-) \rightarrow TiO_2\ (e^-) + Bi_2WO_6$$

$$CO_2 + 8H^+ + 8e^- \rightarrow CH_4 + 2H_2O\ E_0 = -0.24\ V$$

$$2H_2O + 4\ h^+ \rightarrow O_2 + 4H^+\ E_0 = 0.82\ V$$

Table 2 reports a comparison of products yield for some Bi_2WO_6-containing photocatalysts reported in open literature. BT2 as the catalyst with the best performance in the current work shows higher yield in terms of CH_4 production compared with the similar composites reported in the open literature.

4. Conclusions

Bi_2WO_6/TiO_2 photocatalysts with different molar ratios of 1, 2, 3 and 4 were prepared by hydrothermal method and examined in CO_2 photoreduction under visible light irradiation for production of methane. The photocatalyst performances order were BT2 > BT3 > BT4 > BT1 > Bi_2WO_6 > TiO_2, and the highest yield of CH_4 (11.95 μmol/g) was observed for BT2 catalyst. The DRS results indicates that deposition of Bi_2WO_6 nanosheets on TiO_2 nanobelts extended the light absorption of TiO_2 to visible light region. BT2 photocatalyst has the highest visible light absorption efficiency, which is correspond to its smallest bandgap (1.9 eV). Physicochemical and optical properties of photocatalysts shows an enhancement of CO_2 adsorption by the formation of heterojunction photocatalyst. Formation of heterojunction structure between Bi_2WO_6 and TiO_2 is an excellent way to transfer of charge carriers which can prolong the separation time of photoinduced charge carriers which in turn leads to the increment of the photocatalytic performance. In addition, the low recombination rate of electron-hole pairs can enhance the photoconversion efficiency of CO_2.

Author contributions

Maryam Ahmadi: Investigation, Writing (Original draft preparation).

Afsanehsadat Larimi: Project administaration, Resources, Supervision, Conceptualization, Methodology, Funding acquisition, Writing (Reviewing and Editing).

Seyed Mehdi Alavi: Conceptualization, Methodology.

Ethical approval

Not applicable.

Declaration of Competing Interest

The authors have no relevant financial or non-financial interests to disclose.

Data availability

All data generated or analysed during this study are included in this published article.

Appendix A. Supplementary data

Supplementary data to this article can be found online at https://doi.org/10.1016/j.catcom.2023.106681.

References

[1] Z. Jiang, X. Liang, H. Zheng, Y. Liu, Z. Wang, P. Wang, X. Zhang, X. Qin, Y. Dai, M.H. Whangbo, B. Huang, Photocatalytic reduction of CO2 to methanol by three-dimensional hollow structures of Bi2WO6 quantum dots, Appl. Catal. B Environ. 219 (2017) 209–215, https://doi.org/10.1016/j.apcatb.2017.07.023.

[2] W.K. Jo, S. Kumar, S. Eslava, S. Tonda, Construction of Bi2WO6/RGO/g-C3N4 2D/2D/2D hybrid Z-scheme heterojunctions with large interfacial contact area for efficient charge separation and high-performance photoreduction of CO2 and H2O into solar fuels, Appl. Catal. B Environ. 239 (2018) 586–598, https://doi.org/10.1016/j.apcatb.2018.08.056.

[3] L. Cheng, L. Liu, D. Wang, F. Yang, J. Ye, Synthesis of bismuth molybdate photocatalysts for CO 2 photo-reduction, J. CO2 Util. 29 (2019) 196–204, https://doi.org/10.1016/j.jcou.2018.12.013.

[4] J.F.D. Brito, P.G. Corradini, M.V.B. Zanoni, F. Marken, L.H. Mascaro, The influence of metallic Bi in BiVO4 semiconductor for artificial photosynthesis, J. Alloys Compd. 851 (2021), https://doi.org/10.1016/j.jallcom.2020.156912.

[5] L. Liu, K. Dai, J. Zhang, L. Li, Plasmonic bi-enhanced ammoniated α-MnS/Bi2MoO6 S-scheme heterostructure for visible-light-driven CO2 reduction, J. Colloid Interface Sci. 604 (2021) 844–855, https://doi.org/10.1016/j.jcis.2021.07.064.

[6] A. Bazzo, A. Urakawa, Origin of photocatalytic activity in continuous gas phase CO $_2$ reduction over Pt/TiO $_2$, ChemSusChem. 6 (2013) 2095–2102, https://doi.org/10.1002/cssc.201300307.

[7] A. Perazio, G. Lowe, R. Gobetto, J. Bonin, M. Robert, Light-driven catalytic conversion of CO 2 with heterogenized molecular catalysts based on fourth period transition metals, Coord. Chem. Rev. 443 (2021), 214018, https://doi.org/10.1016/j.ccr.2021.214018.

[8] N. Shehzad, M. Tahir, K. Johari, T. Murugesan, M. Hussain, A critical review on TiO 2 based photocatalytic CO 2 reduction system: strategies to improve efficiency, J. CO2 Util. 26 (2018) 98–122, https://doi.org/10.1016/j.jcou.2018.04.026.

[9] Z. Fu, Q. Yang, Z. Liu, F. Chen, F. Yao, T. Xie, Y. Zhong, Photocatalytic conversion of carbon dioxide : from products to design the catalysts, J. CO2 Util. 34 (2019) 63–73, https://doi.org/10.1016/j.jcou.2019.05.032.

[10] A. Francis, S.S. Priya, S.H. Kumar, K. Sudhakar, M. Tahir, A review on recent developments in solar photoreactors for carbon dioxide conversion to fuels, J. CO2 Util. 47 (2021), 101515, https://doi.org/10.1016/j.jcou.2021.101515.

[11] A. Nikokavoura, C. Trapalis, Alternative photocatalysts to TiO2 for the photocatalytic reduction of CO2, Appl. Surf. Sci. 391 (2017) 149–174, https://doi.org/10.1016/J.APSUSC.2016.06.172.

[12] L. Guo, Y. Wang, T. He, Photocatalytic reduction of CO $_2$ over Heterostructure semiconductors into value-added chemicals, Chem. Rec. 16 (2016) 1918–1933, https://doi.org/10.1002/tcr.201600008.

[13] T.P. Yendrapati Taraka, A. Gautam, S.L. Jain, S. Bojja, U. Pal, Controlled addition of Cu/Zn in hierarchical CuO/ZnO p-n heterojunction photocatalyst for high photoreduction of CO2 to MeOH, J. CO2 Util. 31 (2019) 207–214, https://doi.org/10.1016/j.jcou.2019.03.012.

[14] D. Liu, Y. Fernández, O. Ola, S. MacKintosh, M. Maroto-Valer, C.M.A. Parlett, A. F. Lee, J.C.S. Wu, On the impact of cu dispersion on CO 2 photoreduction over cu/TiO 2, Catal. Commun. 25 (2012) 78–82, https://doi.org/10.1016/j.catcom.2012.03.025.

[15] J. Tang, W. Zhou, R. Guo, C. Huang, W. Pan, PT NU, Catal. Commun. (2018), https://doi.org/10.1016/j.catcom.2018.01.006.

[16] H.R. Kim, A. Razzaq, C.A. Grimes, Heterojunction p-n-p Cu2O/S-TiO2/CuO: synthesis and application to photocatalytic conversion of CO2 to methane, J. CO2 Util. 20 (2017) 91–96, https://doi.org/10.1016/j.jcou.2017.05.008.

[17] N. Shehzad, M. Tahir, K. Johari, T. Murugesan, M. Hussain, A critical review on TiO2 based photocatalytic CO2 reduction system: strategies to improve efficiency, J. CO2 Util. 26 (2018) 98–122, https://doi.org/10.1016/J.JCOU.2018.04.026.

[18] A.A. Khan, M. Tahir, Recent advancements in engineering approach towards design of photo-reactors for selective photocatalytic CO2 reduction to renewable fuels, J. CO2 Util. 29 (2019) 205–239, https://doi.org/10.1016/j.jcou.2018.12.008.
[19] M.S. Akple, J. Low, S. Liu, B. Cheng, J. Yu, W. Ho, Fabrication and enhanced CO2 reduction performance of N-self-doped TiO2 microsheet photocatalyst by bi-cocatalyst modification, J. CO2 Util. 16 (2016) 442–449, https://doi.org/10.1016/J.JCOU.2016.10.009.
[20] M. Tasbihi, F. Fresno, I. Álvarez-Prada, A. Acharjya, A. Thomas, L. Escriche, N. Romero, X. Sala, V.A. De La Peña O'Shea, J. García-Antón, A molecular apprfyufhvvoach to the synthesis of platinum-decoratedjffgkfgmdffrgb meso77545875r677667porous graphitic carbon nitride as selective CO2reduction photocatalyst, J. CO2 Util. 50 (2021), https://doi.org/10.1016/j.jcou.2021.101574.
[21] M. Moradi, F. Khorasheh, A. Larimi, Pt nanoparticles decorated Bi-doped TiO2 as an efficient photocatalyst for CO2 photo-reduction into CH4[1] M. Moradi, F. Khorasheh, and A. Larimi, "Pt nanoparticles decorated Bi-doped TiO2 as an efficient photocatalyst for CO2 photo-reduction into CH4", Sol. Energy 211 (2020) 100–110, https://doi.org/10.1016/j.solener.2020.09.054.
[22] R. Nematollahi, C. Ghotbi, F. Khorasheh, A. Larimi, Ni-bi co-doped TiO2 as highly visible light response nano-photocatalyst for CO2 photo-reduction in a batch photo-reactor, J. CO2 Util. 41 (2020), https://doi.org/10.1016/j.jcou.2020.101289.
[23] M. Tahir, Well-designed ZnFe2O4/ag/TiO2 nanorods heterojunction with ag as electron mediator for photocatalytic CO2 reduction to fuels under UV/visible light, J. CO2 Util. 37 (2020) 134–146, https://doi.org/10.1016/j.jcou.2019.12.004.
[24] P.-Q. Wang, Y. Bai, P.-Y. Luo, J.-Y. Liu, Graphene–WO3 nanobelt composite: elevated conduction band toward photocatalytic reduction of CO2 into hydrocarbon fuels, Catal. Commun. 38 (2013) 82–85, https://doi.org/10.1016/j.catcom.2013.04.020.
[25] N. Bao, Z. Yin, Q. Zhang, S. He, X. Hu, X. Miao, Synthesis of flower-like monoclinic BiVO4/surface rough TiO2 ceramic fiber with heterostructures and its photocatalytic property, Ceram. Int. 42 (2016) 1791–1800, https://doi.org/10.1016/j.ceramint.2015.09.142.
[26] J. Yin, Z. Xing, J. Kuang, Z. Li, Q. Zhu, W. Zhou, Dual oxygen vacancy defects-mediated efficient electron-hole separation via surface engineering of Ag/Bi2MoO6 nanosheets/TiO2 nanobelts ternary heterostructures, J. Ind. Eng. Chem. 78 (2019) 155–163, https://doi.org/10.1016/j.jiec.2019.06.021.
[27] B. Tahir, M. Tahir, N.S. Amin, H. Alias, Fabrication of SWCNTs Modified TiO 2 Nanocomposite towards Enhanced Photocatalytic Carbon Dioxide Reduction to Fuels under Visible Light 7, 2019, pp. 343–348, https://doi.org/10.3303/CET1972058.
[28] C. Cao, Y. Yan, Y. Yu, X. Yang, W. Liu, Y. Cao, Modification of Pd and Mn on the surface of TiO $_2$ with enhanced photocatalytic activity for photoreduction of CO $_2$ into CH $_4$, J. Phys. Chem. C 121 (2017) 270–277, https://doi.org/10.1021/acs.jpcc.6b08921.
[29] T.P. Nguyen, D.L.T. Nguyen, V.H. Nguyen, T.H. Le, D.V.N. Vo, Q.T. Trinh, S. R. Bae, S.Y. Chae, S.Y. Kim, Q. Van Le, Recent advances in tio2-based photocatalysts for reduction of co2 to fuels, Nanomaterials 10 (2020) 1–24, https://doi.org/10.3390/nano10020337.
[30] Q. Lu, C. Dong, F. Wei, J. Li, Z. Wang, W. Mu, X. Han, Rational fabrication of Bi2WO6 decorated TiO2 nanotube arrays for photocatalytic degradation of organic pollutants, Mater. Res. Bull. 145 (2022), 111563, https://doi.org/10.1016/j.materresbull.2021.111563.
[31] U. Gaya, Mechanochemical Synthesis and Characterization of N-doped TiO 2 for Photocatalytic Degradation of Caffeine 3, 2018, pp. 29–35, https://doi.org/10.22036/ncr.2018.01.004.
[32] Y. Sang, Z. Zhao, J. Tian, P. Hao, H. Jiang, H. Liu, J.P. Claverie, Enhanced photocatalytic property of reduced graphene oxide/TiO $_2$ nanobelt surface heterostructures constructed by an in situ photochemical reduction method, Small 10 (2014) 3775–3782, https://doi.org/10.1002/smll.201303489.
[33] Q. Alsharari, M. Ray, J. Supervisor, P. Charpentier, Doped TiO2 Nanowires for Applications in Dye Sensitized Solar Cells and Sacrifical Hydrogen Production. https://ir.lib.uwo.ca/etdhttps://ir.lib.uwo.ca/etd/3665, 2016 (accessed July 24, 2018).
[34] G. Yang, D. Chen, H. Ding, J. Feng, J.Z. Zhang, Y. Zhu, S. Hamid, D. W. Bahnemann, Well-designed 3D ZnIn2S4 nanosheets/TiO2 nanobelts as direct Z-scheme photocatalysts for CO2 photoreduction into renewable hydrocarbon fuel with high efficiency, Appl. Catal. B Environ. 219 (2017) 611–618, https://doi.org/10.1016/J.APCATB.2017.08.016.
[35] R. Daghrir, P. Drogui, D. Robert, Modified TiO $_2$ for environmental photocatalytic applications: a review, Ind. Eng. Chem. Res. 52 (2013) 3581–3599, https://doi.org/10.1021/ie303468t.
[36] J. Low, B. Cheng, J. Yu, Surface modification and enhanced photocatalytic CO2reduction performance of TiO2: a review, Appl. Surf. Sci. 392 (2017) 658–686, https://doi.org/10.1016/j.apsusc.2016.09.093.
[37] O. Ola, M.M. Maroto-Valer, Review of material design and reactor engineering on TiO2 photocatalysis for CO2 reduction, J Photochem Photobiol C: Photochem Rev 24 (2015) 16–42, https://doi.org/10.1016/j.jphotochemrev.2015.06.001.
[38] L. Yao, W. Wang, Y. Liang, J. Fu, H. Shi, Plasmon-enhanced visible light photoelectrochemical and photocatalytic activity of gold nanoparticle-decorated hierarchical TiO 2 /bi 2 WO 6 nanorod arrays, Appl. Surf. Sci. 469 (2019) 829–840, https://doi.org/10.1016/j.apsusc.2018.11.031.
[39] X. Song, R. Wang, J. Wang, Z. Huang, S. Ye, D.D. Dionysiou, Construction of TiO2@Bi2WO6 hollow microspheres by template method for enhanced degradation of ethylene under visible light, Opt. Mater. (Amst.) 113 (2021), 110839, https://doi.org/10.1016/j.optmat.2021.110839.
[40] C.S. Ribeiro, J.Z.Y. Tan, M.M. Maroto-Valer, M.A. Lansarin, Photocatalytic reduction of CO2over Bi2WO6in a continuous-flow differential photoreactor: investigation of operational parameters, J. Environ. Chem. Eng. 9 (2021) 0–1, https://doi.org/10.1016/j.jece.2021.105097.
[41] Z. Sun, Z. Yang, H. Liu, H. Wang, Z. Wu, Visible-light CO2 photocatalytic reduction performance of ball-flower-like Bi2WO6 synthesized without organic precursor: effect of post-calcination and water vapor, Appl. Surf. Sci. 315 (2014) 360–367, https://doi.org/10.1016/J.APSUSC.2014.07.153.
[42] C.S. Ribeiro, M.A. Lansarin, Enhanced photocatalytic activity of Bi2WO6 with PVP addition for CO2 reduction into ethanol under visible light, Environ. Sci. Pollut. Res. 28 (2021) 23667–23674, https://doi.org/10.1007/s11356-020-10765-5.
[43] J.H. Lee, H. Lee, M. Kang, Remarkable photoconversion of carbon dioxide into methane using bi-doped TiO2 nanoparticles prepared by a conventional sol-gel method, Mater. Lett. 178 (2016) 316–319, https://doi.org/10.1016/j.matlet.2016.04.193.
[44] X. Huang, J. Zhao, X. Xiong, S. Liu, Y. Xu, Positive effect of Fe3+ ions on Bi2WO6, Bi2MoO6 and BiVO4 photocatalysis for phenol oxidation under visible light, Catal. Sci. Technol. 9 (2019) 4413–4421, https://doi.org/10.1039/c9cy00855a.
[45] J. Wang, L. Tang, G. Zeng, Y. Deng, Y. Liu, L. Wang, Y. Zhou, Z. Guo, J. Wang, C. Zhang, Atomic scale g-C3N4/Bi2WO6 2D/2D heterojunction with enhanced photocatalytic degradation of ibuprofen under visible light irradiation, Appl. Catal. B Environ. 209 (2017) 285–294, https://doi.org/10.1016/j.apcatb.2017.03.019.
[46] Z. Jiao, Y. Tang, P. Zhao, S. Li, T. Sun, S. Cui, L. Cheng, Synthesis of Z-scheme g-C 3 N 4 /PPy/bi 2 WO 6 composite with enhanced visible-light photocatalytic performance, Mater. Res. Bull. 113 (2019) 241–249, https://doi.org/10.1016/j.materresbull.2019.02.016.
[47] Z. Du, C. Cheng, L. Tan, J. Lan, S. Jiang, L. Zhao, R. Guo, Enhanced photocatalytic activity of bi 2 WO 6 /TiO 2 composite coated polyester fabric under visible light irradiation, Appl. Surf. Sci. 435 (2018) 626–634, https://doi.org/10.1016/j.apsusc.2017.11.136.
[48] Z.-H. Wei, Y.-F. Wang, Y.-Y. Li, L. Zhang, H.-C. Yao, Z.-J. Li, Enhanced photocatalytic CO2 reduction activity of Z-scheme CdS/BiVO4 nanocomposite with thinner BiVO4 nanosheets, J. CO2 Util. 28 (2018) 15–25, https://doi.org/10.1016/J.JCOU.2018.09.008.
[49] C. Ma, Z. Xie, W.C. Seo, S.T. Ud Din, J. Lee, Y. Kim, H. Jung, W. Yang, Carbon dot-coupled BiVO4/reduced graphene hydrogel for significant enhancement of photocatalytic activity: antibiotic degradation and CO2 reduction, Appl. Surf. Sci. 565 (2021), 150564, https://doi.org/10.1016/j.apsusc.2021.150564.
[50] X. Zhang, M. Zhang, K. Cao, Hydrothermal synthesis of Sm-doped Bi2WO6 flower-like microspheres for photocatalytic degradation of rhodamine B, CrystEngComm. 21 (2019) 6208–6218, https://doi.org/10.1039/c9ce01043b.
[51] W. Dai, J. Yu, Y. Deng, X. Hu, T. Wang, X. Luo, Facile synthesis of MoS 2 /bi 2 WO 6 nanocomposites for enhanced CO 2 photoreduction activity under visible light irradiation, Appl. Surf. Sci. 403 (2017) 230–239, https://doi.org/10.1016/j.apsusc.2017.01.171.
[52] G. Ren, X. Zhang, C. Zhang, R. Li, J. Liu, Y. Wang, Y. Wang, C. Fan, Q. Zhao, Synergetic effect of Bi2WO6 micro-spheres and activated carbon mm-spheres for enhancing photoreduction activity of CO2 to CO, Mater. Lett. 264 (2020), 127201, https://doi.org/10.1016/j.matlet.2019.127201.
[53] G. Ren, X. Zhang, C. Zhang, R. Li, J. Liu, Y. Wang, Y. Wang, C. Fan, Q. Zhao, Synergetic effect of Bi2WO6 micro-spheres and activated carbon mm-spheres for enhancing photoreduction activity of CO2 to CO, Mater. Lett. 264 (2020), 127201, https://doi.org/10.1016/j.matlet.2019.127201.
[54] X.Y. Kong, W.Q. Lee, A.R. Mohamed, S.P. Chai, Effective steering of charge flow through synergistic inducing oxygen vacancy defects and p-n heterojunctions in 2D/2D surface-engineered Bi2WO6/BiOI cascade: towards superior photocatalytic CO2 reduction activity, Chem. Eng. J. 372 (2019) 1183–1193, https://doi.org/10.1016/j.cej.2019.05.001.
[55] C. Yang, Y. Huang, F. Li, T. Li, One-step synthesis of Bi2WO6/TiO2 heterojunctions with enhanced photocatalytic and superhydrophobic property via hydrothermal method, J. Mater. Sci. 51 (2015) 1032–1042, https://doi.org/10.1007/S10853-015-9433-Y.
[56] M. Zhang, Synthesis of Bi2WO6/TiO2 flake nano-heterostructure photocatalyst and its photocatalytic performance under visible light irradiation, J. Mater. Sci. Mater. Electron. 31 (2020) 20129–20138, https://doi.org/10.1007/S10854-020-04534-W.
[57] G. Colón, S. Murcia López, M.C. Hidalgo, J.A. Navío, Sunlight highly photoactive Bi2WO6–TiO2 heterostructures for rhodamine B degradation, Chem. Commun. 46 (2010) 4809–4811, https://doi.org/10.1039/C0CC00058B.
[58] M. Shang, W. Wang, L. Zhang, S. Sun, L. Wang, L. Zhou, 3D Bi2WO6/TiO2 hierarchical heterostructure: controllable synthesis and enhanced visible photocatalytic degradation performances, J. Phys. Chem. C 113 (2009) 14727–14731, https://doi.org/10.1021/JP9045808/ASSET/IMAGES/MEDIUM/JP-2009-045808_0001.GIF.
[59] S. Murcia López, M.C. Hidalgo, J.A. Navío, G. Colón, Novel Bi2WO6–TiO2 heterostructures for rhodamine B degradation under sunlike irradiation, J. Hazard. Mater. 185 (2011) 1425–1434, https://doi.org/10.1016/J.JHAZMAT.2010.10.065.
[60] H. Li, L. Liang, X. Niu, D. Zhang, H. Fan, K. Wang, Construction of a Bi2WO6/TiO2 heterojunction and its photocatalytic degradation performance, New J. Chem. 46 (2022) 8185–8194, https://doi.org/10.1039/D1NJ06149F.

[61] N. Singhal, R. Goyal, U. Kumar, Over InTaO4: selective methanol formation Visible light assisted photocatalytic CO 2 reduction over InTaO 4: selective methanol formation, 2017, https://doi.org/10.1021/acs.energyfuels.7b02123.
[62] J. Xie, M. Xu, R. Wang, S. Ye, X. Song, Three-dimensional porous spherical TiO2–Bi2WO6 decorated graphene oxide nanosheets photocatalyst with excellent visible light catalytic degradation of ethylene, Ceram. Int. 47 (2021) 14183–14193, https://doi.org/10.1016/j.ceramint.2021.01.286.
[63] R. Wang, M. Xu, J. Xie, S. Ye, X. Song, A spherical TiO2-Bi2WO6 composite photocatalyst for visible-light photocatalytic degradation of ethylene, Colloids Surf. A Physicochem. Eng. Asp. 602 (2020), 125048, https://doi.org/10.1016/j.colsurfa.2020.125048.
[64] Q. Guo, Y. Huang, H. Xu, D. Luo, F. Huang, L. Gu, Y. Wei, H. Zhao, L. Fan, J. Wu, The effects of solvent on photocatalytic properties of Bi2WO6/TiO2 heterojunction under visible light irradiation, Elsevier Masson SAS (2018), https://doi.org/10.1016/j.solidstatesciences.2018.02.013.
[65] L. Ma, J. Duan, B. Ji, Y. Liu, C. Li, C. Li, W. Zhao, Z. Yang, Ligand-metal charge transfer mechanism enhances TiO2/Bi2WO6/rGO nanomaterials photocatalytic efficient degradation of norfloxacin under visible light, J. Alloys Compd. 869 (2021), 158679, https://doi.org/10.1016/j.jallcom.2021.158679.
[66] Y. Li, H. Wang, J. Xie, J. Hou, X. Song, D.D. Dionysiou, Bi2WO6-TiO2/starch composite films with ag nanoparticle irradiated by γ-ray used for the visible light photocatalytic degradation of ethylene, Chem. Eng. J. 421 (2021), 129986, https://doi.org/10.1016/j.cej.2021.129986.
[67] G. Chen, Y. Wang, Q. Shen, X. Xiong, S. Ren, G. Dai, C. Wu, Fabrication of TiO2 nanofibers assembled by Bi2WO6 nanosheets with enhanced visible light photocatalytic activity, Ceram. Int. 46 (2020) 21304–21310, https://doi.org/10.1016/j.ceramint.2020.05.224.
[68] F. Rabanimehr, M. Farhadian, A.R.S. Nazar, M. Moghadam, Fabrication of Z-scheme Bi2WO6/CNT/TiO2 heterostructure with enhanced cephalexin photodegradation: optimization and reaction mechanism, J. Mol. Liq. 339 (2021), 116728, https://doi.org/10.1016/j.molliq.2021.116728.
[69] L. Ji, B. Liu, Y. Qian, Q. Yang, P. Gao, Enhanced visible-light-induced photocatalytic disinfection of Escherichia coli by ternary Bi2WO6/TiO2/reduced graphene oxide composite materials: insight into the underlying mechanism, Adv. Powder Technol. 31 (2020) 128–138, https://doi.org/10.1016/j.apt.2019.10.005.
[70] Z. Liu, X. Liu, D. Lu, P. Fang, S. Wang, Grape-like Bi2WO6/TiO2 hierarchical microspheres: a superior visible light photocatalyst with magnetic recycling property, Mater. Lett. 130 (2014) 143–145, https://doi.org/10.1016/j.matlet.2014.05.097.
[71] Y. Heng Chai, F. Zhou, Z. Zhu, High-efficiency and environment-friendly sterilization PEVE coatings modified with Bi2WO6/TiO2 composites, Chem. Phys. Lett. 715 (2019) 173–180, https://doi.org/10.1016/j.cplett.2018.11.046.
[72] Y. Liu, H. Tang, H. Lv, P. Zhang, Z. Ding, S. Li, J. Guang, Facile hydrothermal synthesis of TiO2/Bi2WO6 hollow microsphere with enhanced visible-light photoactivity, Powder Technol. 283 (2015) 246–253, https://doi.org/10.1016/j.powtec.2015.05.032.
[73] S. Murcia López, M.C. Hidalgo, J.A. Navío, G. Colón, Novel Bi2WO6-TiO2 heterostructures for Rhodamine B degradation under sunlike irradiation, J. Hazard. Mater. 185 (2011) 1425–1434, https://doi.org/10.1016/j.jhazmat.2010.10.065.
[74] Y. Cao, L. Zong, Q. Li, C. Li, J. Li, J. Yang, Solvothermal synthesis of TiO2 nanocrystals with {001} facets using titanic acid nanobelts for superior photocatalytic activity, Appl. Surf. Sci. 391 (2017) 311–317, https://doi.org/10.1016/J.APSUSC.2016.06.198.
[75] W. Li, X. Ding, H. Wu, H. Yang, In-situ hydrothermal synthesis of TiO2/Bi2WO6 heterojunction with enhanced photocatalytic activity, Mater. Lett. 227 (2018) 272–275, https://doi.org/10.1016/j.matlet.2018.05.107.
[76] L. Shiamala, K. Alamelu, V. Raja, B.M. Jaffar Ali, Synthesis, characterization and application of TiO2-Bi2WO6 nanocomposite photocatalyst for pretreatment of starch biomass and generation of biofuel precursors, J. Environ. Chem. Eng. 6 (2018) 3306–3321, https://doi.org/10.1016/j.jece.2018.04.065.
[77] S. Obregón, G. Colón, Erbium doped TiO2-Bi2WO6 heterostructure with improved photocatalytic activity under sun-like irradiation, Appl. Catal. B Environ. 140–141 (2013) 299–305, https://doi.org/10.1016/j.apcatb.2013.04.014.
[78] O. Shtyka, R. Ciesielski, A. Kedziora, W. Maniukiewicz, S. Dubkov, D. Gromov, T. Maniecki, Photocatalytic reduction of CO2 over me (Pt, Pd, Ni, cu)/TiO2 catalysts, Top. Catal. 63 (2020) 113–120, https://doi.org/10.1007/s11244-020-01241-y.
[79] V. Kavinkumar, A. Verma, K. Uma, S. Moscow, K. Jothivenkatachalam, Y.P. Fu, Plasmonic metallic silver induced Bi2WO6/TiO2 ternary junction towards the photocatalytic, electrochemical OER/HER, antibacterial and sensing applications, Appl. Surf. Sci. 569 (2021), 150918, https://doi.org/10.1016/j.apsusc.2021.150918.
[80] X. Sun, H. Zhang, J. Wei, Q. Yu, P. Yang, F. Zhang, Preparation of point-line Bi2WO6@TiO2 nanowires composite photocatalysts with enhanced UV/visible-light-driven photocatalytic activity, Mater. Sci. Semicond. Process. 45 (2016) 51–56, https://doi.org/10.1016/j.mssp.2016.01.015.
[81] M. Sun, Y. Yao, W. Ding, S. Anandan, N/Ti3+ co-doping biphasic TiO2/Bi2WO6 heterojunctions: hydrothermal fabrication and sonophotocatalytic degradation of organic pollutants, J. Alloys Compd. 820 (2020), 153172, https://doi.org/10.1016/j.jallcom.2019.153172.
[82] Y. Xu, J. Yu, J. Long, L. Tu, W. Dai, L. Yang, Z-Scheme Heterojunction of SnS 2 / bi 2 WO 6 for Photoreduction of CO 2 to 100% Alcohol Products by Promoting the Separation of Photogenerated Charges, 2022.
[83] Z. Photocatalysts, X. Liu, G. Liu, A Mini Review on Bismuth-Based, 2023.
[84] L. Yuan, K.Q. Lu, F. Zhang, X. Fu, Y.J. Xu, Unveiling the interplay between light-driven CO2 photocatalytic reduction and carbonaceous residues decomposition: a case study of Bi2WO6-TiO2 binanosheets, Appl. Catal. B Environ. 237 (2018) 424–431, https://doi.org/10.1016/j.apcatb.2018.06.019.
[85] Y. Liu, D. Shen, Q. Zhang, Y. Lin, F. Peng, Enhanced photocatalytic CO2 reduction in H2O vapor by atomically thin Bi2WO6 nanosheets with hydrophobic and nonpolar surface, Appl. Catal. B Environ. (2020), 119630, https://doi.org/10.1016/j.apcatb.2020.119630.
[86] Photocatalytic Reduction of CO2 over Bi2WO6 in a Continuous- Flow Differential Photoreactor Photocatalytic Reduction of CO 2 over Bi 2 WO 6 in a Continuous-Flow Differential Photoreactor: Investigation of Operational Parameters, 2022.
[87] C. Lu, X. Li, Q. Wu, J. Li, L. Wen, Y. Dai, B. Huang, B. Li, Z. Lou, Constructing Surface Plasmon Resonance on bi 2 WO 6 to Boost High-Selective CO 2 Reduction for Methane, 2021, https://doi.org/10.1021/acsnano.1c00452.
[88] T. Chen, L. Liu, C. Hu, H. Huang, Recent advances on bi 2 WO 6 - based photocatalysts for environmental and energy applications, Chin. J. Catal. 42 (2021) 1413–1438, https://doi.org/10.1016/S1872-2067(20)63769-X.
[89] Y. Zhou, Z. Tian, Z. Zhao, Q. Liu, J. Kou, X. Chen, J. Gao, S. Yan, Z. Zou, High-Yield Synthesis of Ultrathin and Uniform Bi 2 WO 6 Square Nanoplates Benefitting from Photocatalytic Reduction of CO 2 into Renewable Hydrocarbon Fuel under Visible Light, 2011, pp. 3594–3601.
[90] X.Y. Kong, Y.Y. Choo, S.P. Chai, A.K. Soh, A.R. Mohamed, Oxygen vacancy induced Bi2WO6 for the realization of photocatalytic CO2 reduction over the full solar spectrum: from the UV to the NIR region, Chem. Commun. 52 (2016) 14242–14245, https://doi.org/10.1039/c6cc07750a.
[91] Y. Li, J. Fan, R. Tan, H. Yao, Y. Peng, Q. Liu, Z. Li, Selective Photocatalytic Reduction of CO 2 to CH 4 Modulated by Chloride Modi fi cation on Bi 2 WO 6 Nanosheets, 2020, pp. 0–9, https://doi.org/10.1021/acsami.0c11551.
[92] S. Murcia-López, V. Vaiano, M.C. Hidalgo, J.A. Navío, D. Sannino, Photocatalytic reduction of CO2 over platinised Bi2WO6-based materials, Photochem. Photobiol. Sci. 14 (2015) 678–685, https://doi.org/10.1039/c4pp00407h.
[93] S. Cao, B. Shen, T. Tong, J. Fu, J. Yu, 2D / 2D Heterojunction of Ultrathin MXene / Bi 2 WO 6 Nanosheets for Improved Photocatalytic CO 2 Reduction 1800136, 2018, pp. 1–11, https://doi.org/10.1002/adfm.201800136.
[94] B. Wo, Q. Wang, K. Wang, L. Zhang, H. Wang, W. Wang, Applied surface science photocatalytic reduction of CO 2 to methane over PtO x -loaded ultrathin, Appl. Surf. Sci. 470 (2019) 832–839, https://doi.org/10.1016/j.apsusc.2018.11.197.
[95] X.Y. Kong, W.Q. Lee, A.R. Mohamed, S.P. Chai, Effective steering of charge flow through synergistic inducing oxygen vacancy defects and p-n heterojunctions in 2D/2D surface-engineered Bi2WO6/BiOI cascade: towards superior photocatalytic CO2 reduction activity, Chem. Eng. J. 372 (2019) 1183–1193, https://doi.org/10.1016/j.cej.2019.05.001.
[96] Z. Xie, Y. Xu, D. Li, S. Meng, M. Chen, D. Jiang, Covalently Bonded Bi 2 O 3 Nanosheet / Bi 2 WO 6 Network Heterostructures for E ffi cient Photocatalytic CO 2 Reduction, 2020, pp. 0–9, https://doi.org/10.1021/acsaem.0c02252.
[97] P. Treatment, Z. Zhang, D. Zhang, L. Lyu, G. Cui, Zekai Zhang Ding Zhang, Lin Lyu, Guokai Cui and Hanfeng Lu, (2022).
[98] Y. Wen Teh, Y. Wei Goh, X. Ying Kong, B.J. Ng, S.T. Yong, S.P. Chai, Fabrication of Bi2WO6/Cu/WO3 all-solid-state Z-scheme composite photocatalyst to improve CO2 Photoreduction under visible light irradiation, ChemCatChem. 11 (2019) 6431–6438, https://doi.org/10.1002/cctc.201901653.
[99] Z. Yang, L. Chen, Y. Yang, Activity Construction of an All-solid-state Artificial Z-scheme System Consisting of Bi 2 WO 6 / Au / CdS Nanostructure for Photocatalytic CO 2 Reduction into Renewable Hydrocarbon Fuel, 2023, pp. 2–10.
[100] X.Y. Kong, W.L. Tan, B. Ng, S. Chai, A.R. Mohamed, Harnessing vis – NIR Broad Spectrum for Photocatalytic CO 2 Reduction over Carbon Quantum Dots-Decorated Ultrathin bi 2 WO 6 Nanosheets 10, 2017, pp. 1720–1731, https://doi.org/10.1007/s12274-017-1435-4.